Check for updates

The Dawning Era of Anticancer Nanomedicines: From First Principles to Application of Silk Nanoparticles

Saphia A. L. Matthew and F. Philipp Seib**

This review introduces nanomedicines and medical silks by addressing seminal and recent research within these fields. First, the successes of nanoparticles in improving the safety profiles and pharmacokinetic–pharmacodynamic properties are explored but also the concepts of threshold dosing and targeting of tumor-associated macrophages. Current barriers to systemic delivery of nanomedicines are detailed and methods to overcome these barriers and increase tumor targeting are evaluated, namely: tuning the nanomedicine size and surface charge for enhanced tumor accumulation and penetration; non-spherical nanomedicine morphologies for macrophage evasion and targeted delivery to endothelial cells; and, surface functionalization for stealth coatings and targeting receptor-mediated endocytosis. The advantages of using silk as a nanomedicine with reference to its structure, composition, biological performance, and formulation are discussed. While batch methods for silk processing enable the formation of nano to microparticles, continuous technology can overcome bottlenecks of the deployed engineering methods such as low throughput and poor reproducibility. Finally, the chemical modification of silk using homogeneous and heterogenous chemistries is assessed within the nanomedicine context. Overall, this review covers silk nanomedicines from first principles to carrier design and on to areas of future development.

1. Introduction

Employing silk in nanomedicines marks a recent advancement, despite the longstanding utilization of other biopolymers, some predating the inception of contemporary nanomedicine terminology in 1991.[1] With an increasing number of nanomedicines successfully transitioning from the bench to the bedside, our appreciation of key milestones on this journey becomes apparent, providing an opportunity to cement them. However, the translational journey of nanomedicines is often convoluted, lengthy, and, in most cases, treacherous. First-in-class designs are particularly vulnerable to falling by the wayside despite their promise. Therefore, there is a need to implement lessons learned to support future developments and devise treatment options to ultimately benefit patients. This review takes us on this journey and connects these milestones with silk nanomedicines.

1.1. Nanomedicine

Nanotechnology encompasses the analysis or manipulation of matter at the nanoscale (1–1000 nm) and can result in the production of nanomaterials with at least one nanoscale dimension.[2] At this scale, the nanostructure size and shape influence the material's physicochemical properties, with a widening of the scope of new material functionality. The application of nanotechnology to medicine has produced the interdisciplinary field of "nanomedicine",[1] which has the overall goal of improving patient quality of life.[3] Nanomedicines, when administered to a stratified patient population, can improve toxicological profiles, control and aid visualization of biodistribution, and increase therapeutic efficacies of lipophilic, immunogenic, or unstable payloads.[4] Due to their unique properties, nanomedicines can stabilize and deliver a broad range of small molecules, proteins, nucleic acids, and imaging agents to target organs, tissues, cells, or subcellular compartments. Nanomedicines can also be designed for intracellular activation, but these must be taken up and trafficked through subcellular compartments to the desired organelle (detailed below).

The creation of nanoparticle tools has already aided medical diagnostics via nanoimaging agents and medical treatments via nanomedicines.[3a,5] To date, approximately 90 nanomedicines and nanoimaging agents are clinically approved,[6] with more

S. A. L. Matthew, F. P. Seib
Strathclyde Institute of Pharmacy and Biomedical Sciences
University of Strathclyde
161 Cathedral Street, Glasgow G4 0RE, UK
E-mail: saphia.matthew@strath.ac.uk; philipp.seib@uni-jena.de

F. P. Seib
Fraunhofer Institute for Molecular Biology & Applied Ecology
Branch Bioresources
Ohlebergsweg 12, 35392 Giessen, Germany

F. P. Seib
Friedrich Schiller University Jena
Institute of Pharmacy
Lessingstr. 8, 07743 Jena, Germany

The ORCID identification number(s) for the author(s) of this article can be found under https://doi.org/10.1002/adtp.202400130

© 2024 The Author(s). Advanced Therapeutics published by Wiley-VCH GmbH. This is an open access article under the terms of the Creative Commons Attribution License, which permits use, distribution and reproduction in any medium, provided the original work is properly cited.

DOI: 10.1002/adtp.202400130

than 60% of the commercially available products consisting of lipid-based and nanocrystal formulations[6] by virtue of their greater drug-loading capacities compared to polymeric, protein-based, inorganic, and composite nanocarriers.[4a,6] Drug delivery remains the major application of clinical nanomedicine and research and now provides treatment options for diseases ranging from cancer (e.g., liposomal doxorubicin Doxil, liposomal cytarabine plus daunorubicin in a synergistic 5:1 molar ratio Vyxeos, and recombinant fusion protein d'enileukin diftitox Ontak) to anemia (e.g., polymer-protein conjugate Mircera).[7] Inorganic metallic and metal oxide nanoparticles are potential imaging and therapeutic platforms, although Food and Drug Administration (FDA) approval has so far been limited to iron and superparamagnetic iron oxide nanoparticles (e.g., Feraheme, NanoTherm).[4a,6] Nevertheless, the early research and development pipeline for inorganic nanoparticles remains active; for example, silica quantum dots and gold nanoparticles for imaging have reached clinical trials (phase I/II) to validate safety and efficacy before commercialization.[4a,6,8]

Further advancement of nanomedicine coalesces in situ diagnosis and treatment via "nanotheranostics." This concept requires multi-functional therapeutic nanocarriers that can accumulate in the organ of interest and exhibit responsiveness to the disease-state by emitting a monitorable signal alongside payload release.[3a,9] In cancer therapy, this offers a method for patient stratification as it enables screening of tumor uptake of the nanocarrier, thereby ensuring that each patient receives an appropriate treatment plan.[3a,7d] Yet, with no clinical approvals to date, nanotheranostic agents remain in their infancy. At present, only a dozen or so products in various stages of clinical trials are listed in the World Health Organization's International Clinical Trials Registry Platform.

For both diagnosis and treatment, clinical nanomedicine has provided advantages over traditional small-molecule therapies and conventional diagnostic modalities. The pharmacokinetic and pharmacodynamic properties of nanomedicine are dictated by the carrier at the moment the drug becomes bound to or is encapsulated by the carrier. The physicochemical, geometrical, and mechanical properties of the carrier can then be tuned to reduce the adverse systemic effects of small-molecule therapies and increase the sensitivity of diagnostic modalities.[8,10] Further improvements, particularly within the realms of multi-functionality and large-scale GMP manufacture, highlight the promise this field harbors. Regardless, multiple hurdles remain, including multi-drug cancer resistance, targeted delivery, quality control of lab-scale nanomedicine production, and reproducible scale-up to GMP manufacture.[7d,8a,11] Consequently, this review will summarize the rationale for and advantages of therapeutic silk nanomedicines, specifically in the treatment of cancer.

1.1.1. Therapeutic Delivery to Tumor Environments

The original promise of cancer nanomedicines was to provide a "magic bullet" that would target tumors passively through the circulatory system following systemic administration while reducing off-target side effects from classic chemotherapy.[12] This idea now utilizes the paradigm of the enhanced permeability and retention (EPR) effect discovered in 1986.[13] The EPR effect proposed that nanoparticles extravasate through large inter-endothelial gaps into solid tumors and are retained there due to the tumor's poor lymphatic drainage.[14]Cancer nanomedicines that use passive targeting have shown some success,[7a,c,15] with fourteen systemically administered anticancer nanomedicine agents now approved for clinical use. The majority of these are liposomal nanoformulations of off-patent, small-molecule cytotoxic agents that display improved pharmacokinetics and reduced toxicity compared to the free forms of the same drugs.[7d,14a,16] For example, patients treated with PEGylated liposomal doxorubicin (Doxil) experience less cardiotoxicity, less hair loss, a five-fold greater tumor exposure half-life of the drug, and three orders of magnitude prolonged clearance compared to patients treated with free doxorubicin.[16,17] The improved tolerance to liposomal doxorubicin and longer drug dosing compared to free doxorubicin also make Doxil suitable for incorporation into combination therapy regimens.[16] However, the clinical efficacy of many cancer nanomedicines and survival rates compared to the free-form drugs have not lived up to initial expectations.[14a] The poor improvement in efficacy is due in part to the reformulation of clinically approved cytotoxic agents, which means that the mechanism of action and vulnerability to drug resistance may remain the same as the free drugs already on the market.[17] However, reformulated drugs can also change their uptake routes into cells, thereby providing a new opportunity for overcoming multidrug-resistant mechanisms[18] as well as for changing their pharmacological responses. Therefore, each and every system needs individual assessment for its clinical merit.

A now recognized barrier to improved efficacy is that the EPR effect is not omnipresent in humans, unlike the situation in typical rodent tumor models that have been carefully selected to show a robust EPR effect.[14a] Advances in imaging technologies have confirmed that active endothelial transcytosis is an important route that perhaps also plays a more prominent role in nanoparticle extravasation in human tumors than had previously been anticipated.[14a]

The capacity of passively targeted nanomedicines to accumulate in human tumors is still not fully established.[19] For example, Wilhelm et al. reported in 2016 that only ≈0.7% of the injected doses of various nanomedicines accumulate in the tumor following systemic administration.[20] However, this result conflicts with the outcome of a 2001 clinical trial in which more than 0.7% of the injected dose of radiolabeled liposomes accumulated in the solid tumors of 83% of the recruited patients.[7b,21] Indeed, Lammers et al.[16] argue that the proportion of an injected dose that accumulates in the tumor versus off-target sites has a larger influence on the drug's benefit to patients, suggesting that normalizing the tumor-accumulated dose by unit weight of tissue would provide a more useful measure of tumor accumulation.[16] Lammers[19] also reasons that the absolute number of nanoparticles administered also influences the tumor delivery and treatment efficacy, based on in vivo results reported by Ouyang and colleagues,[22] who demonstrated that a threshold dose of 10^{12} nanoparticles per injection per mouse was required to overwhelm the uptake by phagocytic Kupffer cells in the liver. Supplying a drug above this threshold dose results in lower hepatic clearance rates, longer circulation times, and greater tumor accumulation.[22] Indeed, applying an extrapolated dosing threshold of 1.5×10^{15} nanoparticles per injection per human patient is supported by the success of nanomedicines administered above this threshold compared to those administered at lower doses.[19] These studies demonstrate that a holistic approach is needed, with a fresh look taken at each and every step from nanomedicine design to therapeutic use.

Other hurdles that hinder nanoparticle tumor accumulation and penetration arise due to the physiological features of the tumor microenvironment, including its low interstitial pH and hypoxia,[23] dense interstitial matrix, higher interstitial fluid pressure, and irregular tumor vascularization due to cancer cell hyperplasia.[18] The leaky tumor blood vessels may reduce the opportunities for nanomedicines to enter the tumor, whereas the higher interstitial fluid pressure may lower the diffusion rate between the interstitium and intravascular space by lowering the fluid pressure gradient.[20b] In addition, the concentration of tumor-associated macrophages can be highest near the tumor blood vessel, as reported for SKOV-3 xenograft CD1 nude mouse models bearing solid tumors.[20a] The 2D immunofluorescent histopathology analysis conducted in that study demonstrated that 70% of tumor blood vessels were associated with perivascular tumor–associated macrophages, and this localization of tumor-associated macrophages near the tumor vasculature meant a high likelihood of premature nanoparticle phagocytosis upon extravasation.[20a] For example, Miller et al.[24] used intravital imaging, flow cytometry, and histology studies in an HT-1080 xenograft mouse model to follow drug distributions 24 h after intravenous administration of a 100 nm poly(lactic-*co*-glycolic acid)-polyethylene glycol-BODIPY carrier encapsulating a platinum(IV)-BODIPY payload. Their analysis[24] revealed that even though tumor-associated macrophages only comprised ≈4% of the tumor cell population, they internalized more than 30% of the systemically administered nanoparticle dose.[24] Relative to tumor cells, this equated to tumor-associated macrophages internalizing 40% of the total nanoparticle dose. The authors also reported that, on a per cell basis of the bulk tumor, the tumor-associated macrophages took up the greatest number of nanoparticles and accumulated the greatest payload. Increased uptake into leukocytes near the tumor vasculature was corroborated by imaging uptake of the carrier in tumor-bearing fractalkine Cx3cr1GFP/ þ reporter mice.[24]

Nanoparticle uptake by tumor-associated macrophages may also play a role in tumor shrinkage, due to the role of these cells in significantly increasing nanoparticle delivery to the tumor, releasing their payload to neighboring cancer cells,[24] and migrating to metastatic tumor sites.[25] These are important considerations and the first in vitro studies have shown silk nanomedicine effects on macrophages.[26] However, more work is needed, including dedicated in vivo studies. Using intravital imaging and flow cytometry, Miller et al.[24] reported that administration of a platinum(IV)-BODIPY payload to the HT-1080 xenograft mouse model resulted in better drug distribution throughout the tumor tissue compared to the 100 nm poly(lactic-*co*-glycolic acid)-polyethylene glycol-BODIPY carrier. Their flow cytometry data also indicated that the payload was transferred from tumor-associated macrophages to tumor cells, as more than double the payload compared to the carrier accumulated in the tumor cells. Histology and intravital imaging also pointed to almost threefold higher payload concentrations, within roughly one cell-length of tumor-associated macrophages despite the vehicle concentration remaining unelevated. Consequently, DNA damage in the tumor cells was greatest within the phagocyte-neighboring region.[24] Another study that used fluorescence microscopy and flow cytometry in an orthotopic murine glioma model showed that macrophages took up ≈60–80% of the total cyclodextrin-based nanoparticles delivered by intracranial and intravenous administration.[25] Strikingly, the macrophages that took up nanoparticles migrated into circulation and settled in metastatic tumors.[25]

The nanomedicine accumulation sites are therefore key factors that determine their therapeutic efficacy, including their ability to overcome tumor multidrug resistance. The physiological features of the tumor microenvironment, in tandem with cellular features like plasma membrane pumps, can cause multidrug resistance by causing the nanomedicine to accumulate at the periphery of the tumor and fail to penetrate deeper into the tumor.[20b] These physiological barriers to payload delivery are further exacerbated by the chemical features of the tumor microenvironment, which can be characterized by faulty apoptotic mechanisms and the over-expression of efflux transporters, which can lower the drug efficacy following its delivery to the target tumor cells.[20b,27] Hence, understanding the endocytotic pathways by which nanomedicines are trafficked in both cancer and healthy cells is a precondition for improving nanomedicine uptake by cancer cells and ensuring the delivery of a drug payload to the cancer cell's target intracellular organelle or receptor.

1.1.2. Endocytosis: A Gateway for Nanomedicines

Endocytosis is one of the cellular pathways used for the uptake of extracellular material and the maintenance of cell homeostasis by macropinocytosis, phagocytosis, and receptor-mediated endocytosis (**Figure 1**).[3b,4b,28] This is accomplished through the internalization of extracellular fluid, the cellular membrane, and incorporated components, including surface signaling receptors and antigens.[29] The process begins with absorption of matter bound to the plasma membrane in endocytic vesicles, which form by the "pinching off" of membrane invaginations (Figure 1).[4b] The membrane-enclosed cargo is then trafficked to the early endosome, which acts as the cell "sorting station." From there, intracellular transport becomes dependent on the nature of the endosome cargo, with recycling routes available via exosome biogenesis. From the late endosome, escape routes are accessible through the retrieval of cargo into the cytoplasm.[4b] Transport to the lysosomes can offer a further breakdown route through lysosomal enzyme degradation,[30] as these membrane-bound organelles have an acidic pH and contain degradative hydrolase enzymes.[29,31] In polarized cells, cargo transport across the poles can also occur in a process termed "transcytosis".[4b]

Nanoparticle internalization may occur via membrane fusion with fusogenic carriers or through multiple trafficking pathways, notably macropinocytic, clathrin-independent/dynamin-independent-mediated, caveolin-mediated, fast endophilin-mediated, clathrin-mediated, and phagocytic endocytosis. Macropinocytosis involves the endocytosis of fluids and particles of up to ≈1 μm in diameter in the bulk phase by actin polymerization, which mediates membrane-ruffling macropinosome fission.[28,32] Due to the similarity of macropinocytosis

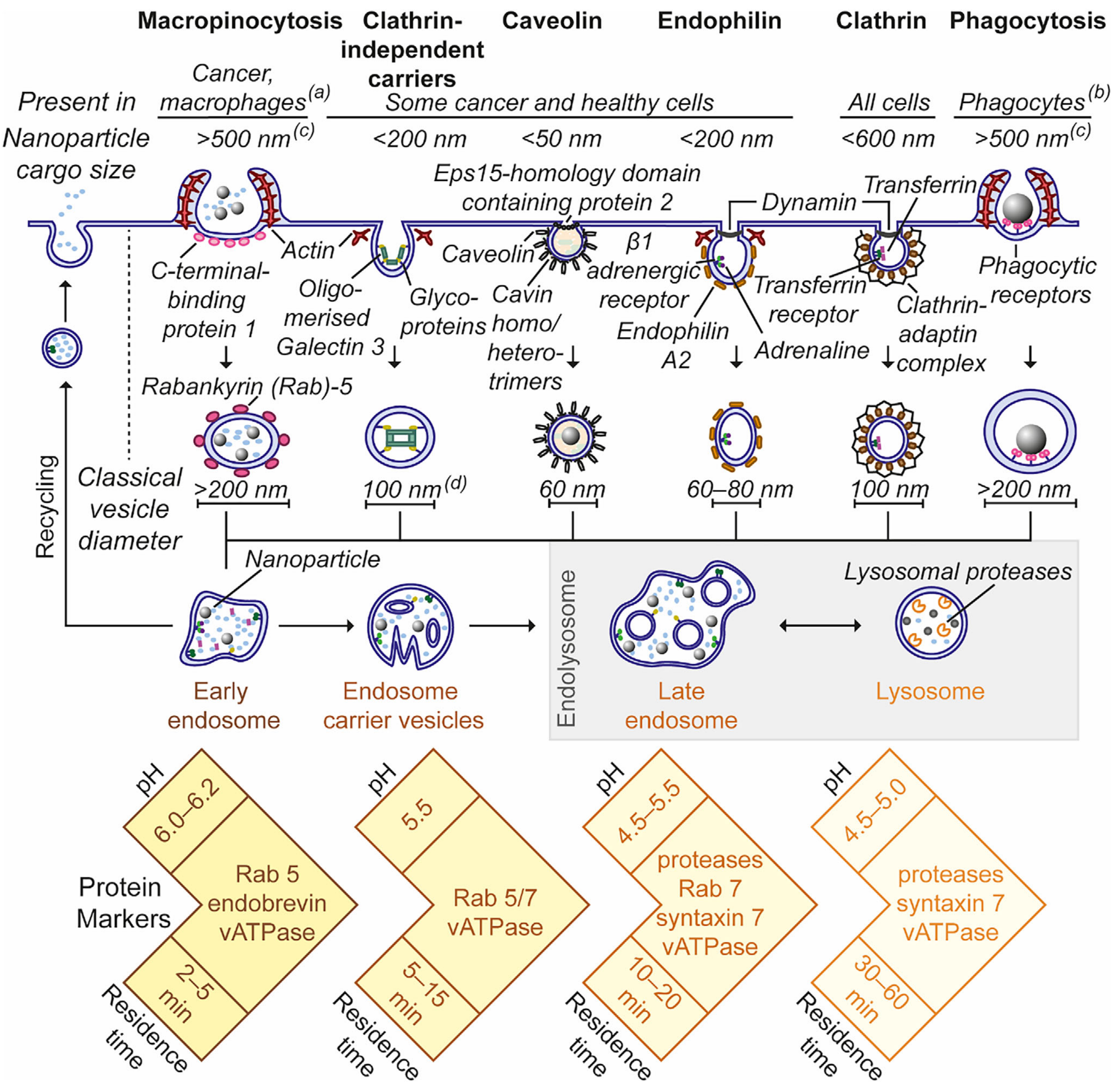
Macropinocytosis
Clathrin-independent carriers
Caveolin
Endophilin
Clathrin
Phagocytosis
Present in
Cancer, macrophages(a)
Some cancer and healthy cells
All cells
Phagocytes(b)
Nanoparticle cargo size
>500 nm(c)
<200 nm
<50 nm
<200 nm
<600 nm
>500 nm(c)
Eps15-homology domain containing protein 2
Dynamin
Transferrin
C-terminal-binding protein 1
Actin
Oligo-merised Galectin 3
Glyco-proteins
Caveolin
Cavin homo/hetero-trimers
β1 adrenergic receptor
Endophilin A2
Transferrin receptor
Adrenaline
Clathrin-adaptin complex
Phagocytic receptors
Rabankyrin (Rab)-5
Recycling
Classical vesicle diameter
>200 nm
100 nm(d)
60 nm
60–80 nm
100 nm
>200 nm
Nanoparticle
Endolysosome
Lysosomal proteases
Early endosome
Endosome carrier vesicles
Late endosome
Lysosome
Protein Markers
pH
6.0–6.2
Rab 5
endobrevin
vATPase
2–5 min
Residence time
pH
5.5
Rab 5/7
vATPase
5–15 min
Residence time
pH
4.5–5.5
proteases
Rab 7
syntaxin 7
vATPase
10–20 min
Residence time
pH
4.5–5.0
proteases
syntaxin 7
vATPase
30–60 min
Residence time

Figure 1. Nanomedicine endocytic and membrane recycling pathways in mammalian cells. The typical organelle pH,[28,30,31b,32] main organelle marker proteins,[28,32] and residence times[28] of nanoparticles within each organelle are shown at the bottom of the diagram. a) Macropinocytosis is upregulated in cancer cell lines expressing oncogenic Ras,[32,33] macrophages, endothelial cells, and epithelial cells in the presence of growth factors or pathogens and has been implicated in neuronal axon growth and the immune protection mechanisms of microglia. b) Non-professional phagocytic cells may be unable to utilize their phagocytic machinery as they do not express the phagocytic receptors required to bind extracellular cargo.[32] Phagocytic receptor gene knock-in human epithelial cells were capable of phagocytosis.[34] c) Some studies have shown that these pathways can be utilized for particles with diameters as small as 50 nm.[28,32] d) The vesicle diameters formed by the clathrin-independent/dynamin-independent pathway utilizing clathrin-independent carriers for early endosomal compartments enriched in glycosylphosphatidylinositol-anchored proteins are generally similar to the vesicle diameters of the clathrin-mediated and fast endophilin-mediated endocytosis pathways.[28,33,35] The depicted pathways typically derived from in vitro studies. Image adapted from refs. [28, 32, 33].

to phagocytosis[28] and clathrin-independent/dynamin-independent-mediated endocytosis, the potential for in vivo internalization of nanoparticles by macropinocytosis is unclear.[32] The process is constitutively present in macrophages and dendritic cells to enable them to readily identify pathogens[35] and it is upregulated in some cancer cell lines[32,33] to facilitate the transport of nutrients, growth factors, and inorganic salts required for cell metabolism.[36] This pathway provides a drug delivery target for cells expressing oncogenic Ras and is upregulated compared to its activity in the healthy counterparts.[33]

In mammalian cultured cells, clathrin-independent/dynamin-independent-mediated endocytosis is constitutive and is associated with nanoparticles less than 200 nm in diameter due to the small tubule opening.[28,32] The mechanism begins with the adsorption of extracellular Galectin 3 to membrane glycoproteins and glycolipids, followed by polymerization of Galectin 3 and finally actin and other proteins to control tubule fission.[32] Caveolin-mediated endocytosis has been proposed for fatty acid transport in adipocytes, endothelial cells, muscle cells, and some cancer cells that bear the required cytosolic caveolin, extracellular cavin proteins, and the Eps15-homology domain-containing protein 2 to form the flask-like caveolae.[28,32,37] However, the small 50 nm opening of the caveolae and the poor specificity of inhibitors for this pathway create questions regarding the extent to which nanoparticles can be internalized by caveolae.[28,32] Fast endophilin-mediated endocytosis has been proposed for cargoes below 200 nm in diameter in some healthy and cancer cells.[32,33] The dynamin-dependent process is driven by a number of ligand-receptor interactions, such as endophilin A2 with membrane receptors. Actin polymerization enables the formation of tubules several hundred nanometers long, while membrane scission is dependent on dynamin.[32]

Clathrin-mediated endocytosis is also a dynamin and energy-dependent process that contributes to fluid phase endocytosis for all cells,[32,38] and has been implicated in multiparticle endocytosis of nanoparticles ranging in size from 30–550 nm.[28] The clathrin-coated pits can stretch to diameters of ≈600 nm around particle aggregates and are formed by binding of cytosolic adaptins, cytosolic clathrin, and extracellular transferrin to transferrin membrane receptors. Phagocytosis is similarly a receptor-driven process, but it is limited to specialized phagocytes that express the phagocytic membrane receptors that tightly bind opsonized extracellular substances and are not typically found in cancer cells.[28,32,33] In micropinocytosis, actin polymerization and membrane ruffling mediates phagosome fission. Internalization of a range of nanoparticle sizes, from ≈3 µm to 50 nm in diameter, has been suggested for phagocytosis. Ultimately, hybrid pathways may also be present, operating by hijacking parts of the classical pathways. Consequently, the endocytic pathway observed for one cell type in vitro may differ from what is later observed by in vivo analysis.[28,32]

The selective trafficking of nanocarriers and their low-molecular-weight, weakly basic payloads to the lysosome was first reported in 1972 by Trouet et al. for a DNA-daunorubicin complex.[39] Trafficking to the lysosome was subsequently coined “lysosomotropic delivery” by De Duve et al. and this has become a characteristic of successful drug delivery systems as this route evades drug efflux.[40] The discovery led De Duve to propose piggyback endocytosis in 1974 as a rationale for targeting specific intracellular trafficking pathways by exploiting the property of a specific nanomedicine rather than the payload (**Figure 2**).[40,41] Piggyback endocytosis has remained a focus of drug delivery for more than 50 years and has ultimately resulted in clinically approved lysosomotropic anticancer nanomedicines, such as Doxil[7a,42] and Abraxane,[7c,42] which are used as second-line therapies for chemotherapy-resistant breast tumors.[38a]

An understanding of the relationship between each nanomedicine and the endocytic route observed in vitro and in vivo in relevant cell models is vital for increasing clinical applicability.[38a] For instance, the success of lysosome-targeted delivery of a nanomedicine hinges on its many physicochemical and biological properties, including carrier biocompatibility, preferential internalization by the target cells, stability of the payload to acidic pH and lysosomal enzyme action, and pH-responsive release of the payload from the carrier.[3b,40] Poor nanomedicine properties can limit efficacy and increase systemic toxicity due to biological effects, such as low cytoplasmic release of the cargo from the endosome and cargo efflux to the extracellular medium by membrane-bound pumps, respectively.[40,43]

For example, live cell microscopy of murine B16BL6 melanoma cells and human BLM melanoma cells demonstrated uptake and lysosomal sequestration of Doxil, which was linked to lower in vitro cytotoxicity and intracellular bioavailability compared to free doxorubicin.[44] Lysosomotropic delivery of Doxil was also observed in vivo using high resolution intravital imaging of mice bearing B16BL6 or BLM dorsal skinfold chamber tumors. In the absence of the liposomal carrier, doxorubicin diffused rapidly through the cytoplasm to the nucleus, whereas entrapment within the stable liposomal carrier prevented extracellular doxorubicin release and predominantly resulted in drug trafficking to the lysosomes. The authors hypothesized that the membrane permeability of doxorubicin is reduced by protonation within the lysosomes. The consequent slow intracellular release into the cytoplasm contributes to the lower therapeutic value of Doxil compared to free doxorubicin.[44] However, comparable in vivo studies have not been reported with silk nanomedicines.

The careful molecular design of nanomedicines can increase the cargo half-life and cytosol accumulation by the incorporation of endosomal escape units that weaken the endosomal membrane, thereby protecting payloads from degradation by hydrolytic enzymes or acidic pH and allowing the payload to travel through the cytoplasm to the target cell compartment.[40,45] Multiple endosomal escape mechanisms have been identified, including the ‘proton sponge effect’ in which the carrier molecules become protonated in the endosome. This causes an influx of chloride ions, osmotic swelling, and membrane rupture, followed by membrane fusion of liposomal carriers with the endosome, mediated by ion pairing between cationic carrier lipids with anionic endosomal lipids, pore formation in the endosomal membrane by self-assembling peptides, and membrane disruption by polymers or peptides that interact with the endosomal membrane.[45b] Lipid nanoparticle endosomal escape units used with liposomal and lipid carriers have included lipid dioleoylphosphatidylethanolamine for membrane fusion-based escape and pH-responsive or cationic lipids for proton sponge-based escape. The nanoparticle endosomal escape units fabricated from polymers and peptides have also been used to incorporate pH-responsiveness and multiple cationic charged sequences, such as poly-histidine peptides.[45a]

Although targeting receptor-mediated endocytosis can result in enhanced uptake, the physicochemical properties of the protein corona and nanoparticle can interfere with ligand-receptor binding. For example, due to the size limit of 50 to 60 nm for caveolae-based vesicles, this route is inherently favored by smaller nanoparticles, as reported for the uptake of gold nanoparticles in HepG2 cells and for polystyrene nanoparticle uptake in HUVEC cells.[37] In addition, understanding of the endocytic

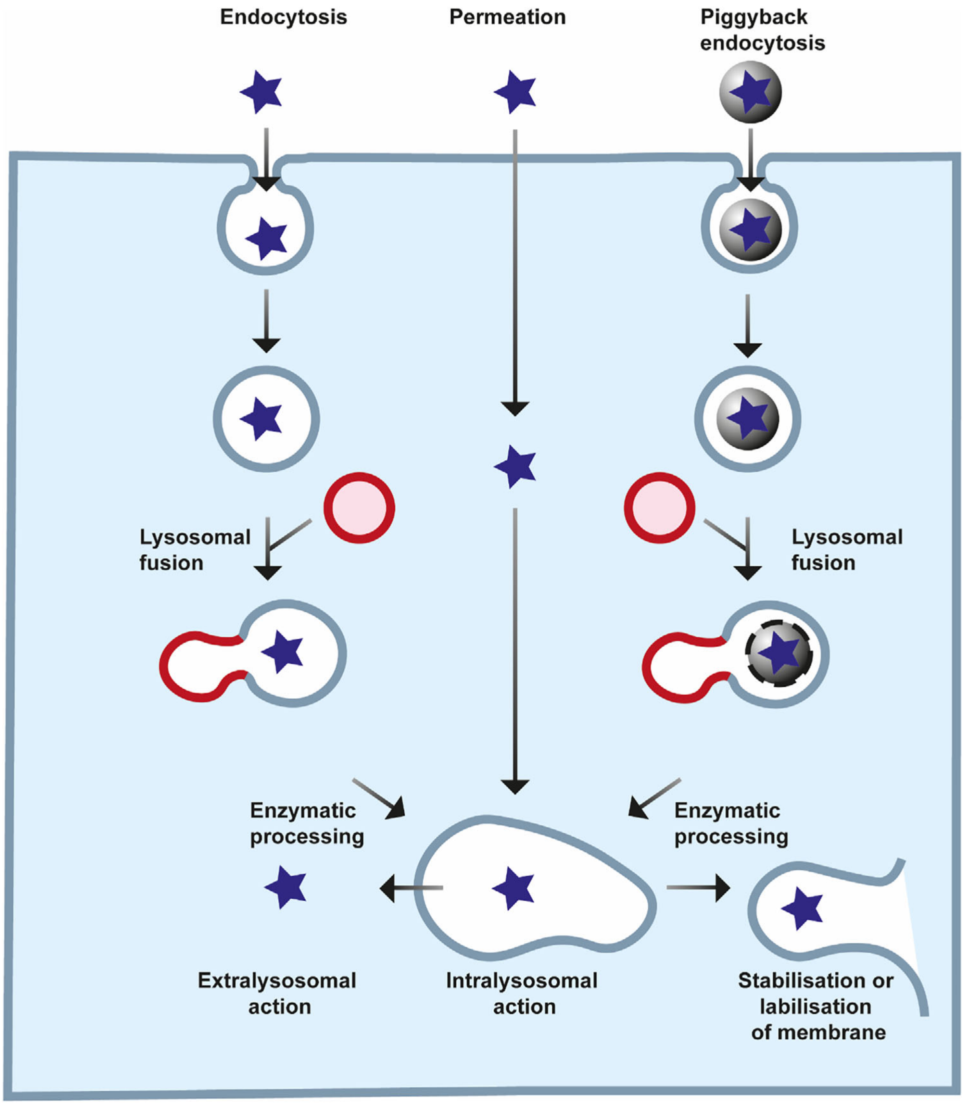

Figure 2. Lysosomotropic delivery via endocytosis, piggyback endocytosis, and permeation cell entry routes. Adapted from De Duve et al.[40]

uptake for both native and therapeutically loaded nanoparticles is crucial to ensure payload delivery to the desired organelle, as transport mechanisms and rates can differ upon therapeutic loading. This was exemplified by variants of in recombinant spider silk nanoparticles, including polyanionic eADF4(C16). Following the loading of polycationic species by electrostatic adsorption, cellular uptake increased almost twofold compared to the native nanoparticles in response to changes in the physicochemical properties, such as surface charge and hydrophilicity.[46]

2. Cancer-Targeted Nanomedicine

Two of the primary obstacles that hinder the clinical translation of current cancer nanomedicines arise from the heterogeneous biology of tumors among patients and the complexity of the physiological response to nanomedicines.[10b] Consequently, patient stratification has been proposed as a method for matching nanoformulations with tumor heterogeneity.[14b] For example, the EPR effect and tumor microenvironment vary significantly between patients and tumor types; therefore, several preliminary clinical studies have proposed using non-invasive imaging to stratify the subpopulations of cancer patients for which nanoparticle accumulation via the EPR effect is likely.[11a,47] This type of work would provide predictive markers for patients who would benefit from passively targeted nanoparticles and expedite targeted treatment to the patients who require it.[10b,11a]

Further objectives include the identification of mechanisms by which tumor size can be reduced so that cellular or acellular targets can be identified and targeted. Pertinent examples include tumor-associated macrophage depletion and extracellular matrix degradation as co-injection or sequential injection schemes to increase nanoparticle targeting to cancer cells.[20a] The chemoattraction of macrophages and other immune cells to tumor sites is useful for targeted delivery of nanoparticles, especially to hypoxic regions distant from blood vessels, as this does not rely on passive accumulation. This strategy has been used in nu-

Table 1. The impact of nanoparticle surface charge, described by the zeta potential, on biodistribution, toxicity, tumor penetration, and internalization by cancer cells.

Biological impact				Refs.
Biodistribution	Toxicity	Tumor penetration	Cancer cell internalization	
←10 mV and >+10 mV: rapid hepatic and mononuclear phagocytic system clearance ±10 mV: lower hepatic clearance, longest circulation times >0 mV: early lung accumulation	>+10 mV: hemolysis, cytotoxic	Pore size ≈ Debye length: electrostatic interaction with tumor vessel, poor extravasation Lower zeta potential: faster matrix diffusion	←10 mV: lower uptake than cations >0 mV: adsorption-mediated endocytosis and lysosomal escape	[20b,50–53]

merous studies; for example, in the use of macrophages loaded with gold nanoshells to infiltrate tumor spheroids in vitro[48] and in murine metastatic breast cancer in vivo.[49] Alternative pretreatment strategies to increase the efficiency of nanoparticle delivery to cancer cells include the use of external stimuli, such as hyperthermia and radiation, vascular normalization, extracellular matrix modification, photodynamic therapy, and chemotherapy priming.[47b]

Overchuk and Zheng suggest that nanoparticle delivery and intra-tumoral behavior should also be thoroughly investigated in the pre-clinical stages.[47b] Quantifying targeting efficiency and correlating it with therapeutic efficacy would enable a standardization between modalities for comparison.[20a] Currently, most preclinical studies analyze the gross accumulation and subtumoral localization of the active pharmaceutical ingredient using available analytical techniques, such as mass spectrometry, high-performance liquid chromatography, gamma counting, and fluorescent microscopy with histology. Intracellular uptake analysis with optical tissue clearing techniques is more beneficial than flow cytometry for parsing nanoparticle spatial distribution with respect to cancer cells and vascular structures at single-cell resolution. Intravital microscopy can also enable in situ evaluation of tumor microenvironmental changes with time in the same animal.[47b]

3. Physicochemical Properties of Nanoparticles

The size and surface charge of nanomedicines can modulate their stealth properties in the circulatory system and alter their cellular interactions at the tumor site.[20b] The surface charge of nanomedicines mainly dictates the rate of clearance by the immune system and liver (**Table 1**).[50] For example, cationic nanomedicines with zeta potentials above +10 mV are cytotoxic, induce hemolysis, interact with serum constituents, undergo rapid clearance by the mononuclear phagocytic system in the bloodstream, and undergo rapid hepatic clearance, resulting in systemic cytotoxicity and a short circulation half-life.[20b,51] By contrast, anionic nanomedicines with zeta potentials below −10 mV show lower cellular uptake than cationic nanomedicines but also cause rapid mononuclear phagocytic system clearance and rapid hepatic clearance.[20b,50,51] The biodistribution of liposomal nanomedicines to the lungs has shown charge-dependency following intravenous administration to male BALB/c mice.[52] Only cationic formulations showed greater accumulation in the lungs at 3 min post-injection compared to the blood plasma, spleen, kidney, and liver, possibly due to the aggregation of liposomes with blood cells which then lodge in the lung capillaries.[52]

Cationic nanomedicines can exhibit non-specific cytotoxicity in the systemic circulation, and Weiss et al. suggest that surface charge density, which can be described by electrokinetic charge, may be a more accurate measure of toxicity than zeta potential.[53a] The authors conducted in vitro 24 h treatments of THP-1-derived macrophages and airway epithelial cells (A549 and Calu-3) with cationic carbon nanoparticles of similar zeta potential (+20.6 to +26.9 mV) but increasing electrokinetic charges (0.23 to 4.39 μmol g^{-1}).[53a] The in vitro cell viability of all cell types decreased as the electrokinetic charge increased, and only the nanoparticles with the two highest electrokinetic charges significantly caused oxidative stress, elevated IL-8 levels, mitochondrial perturbation, and lysosome damage in THP-1 cells. This finding was reinforced in vivo whereby intranasal administration of the two nanoparticle species with the two highest electrokinetic charges caused inflammation of the airways 24 h post-installation in healthy mice.[53a]

Neutral nanomedicines with zeta potentials ≈±10 mV have the longest circulation but the lowest colloidal stability in the absence of adsorption of an electrostatic or steric stabilizer.[20b,51] For example, in CD-1 male mice, the liver uptake of radiolabeled liposomes containing negatively charged phospholipids (180–186 nm, zeta potentials below −39 mV) was ≈40–50% of the injected dose g^{-1} at 0.25 h post-injection, compared to ≈20–30% uptake of the injected dose g^{-1} of plain and slightly positively charged liposomes (188–226 nm, zeta potentials −9.64 and +8.48 mV, respectively).[53c] The greater hepatic uptake of negatively charged liposomes at 0.25 h contributed to the observed increase in clearance from the circulatory system for the negatively charged liposomes (>90% of the injected dose g^{-1}) compared to the neutral liposomes (<70% of the injected dose g^{-1}).[50,53c]

The nanoparticle surface charge impacts extravasation from tumor blood vessels into the tumor microenvironment through the pores of the endothelium membrane.[50] Electrostatic interaction with the negatively charged surface of the tumor vessel walls is significant when the diameter of the pores in the endothelia and the nanoparticle Debye length are similar.[53b] When pore sizes are smaller than the Debye length, hydrodynamic and steric repulsion mainly contribute to poor extravasation. Conversely, when pore sizes are larger than the Debye length all repulsive forces decrease. As vessel pore size can vary between organs, the ability of a nanoparticle species to extravasate into the tumor is also dependent on the cancer sub-type.[53b] Within the tumor, diffusion through the interstitial fluid is easier for nanomedicines

Table 2. The impact of nanoparticle size on biodistribution, toxicity, tumor penetration, and internalization by cancer cells.

Biological impact				Refs.
Biodistribution	Toxicity	Tumor penetration	Cancer cell internalization	
<200 nm: reduced clearance by reticuloendothelial system <20 nm: increased renal clearance Average accumulation order of different-sized nanoparticles, from high to low: liver, spleen, tumor, other tissues	<100 nm: increased hemolysis in vitro	<20 nm: greater transvascular transport and longer matrix diffusion length 20–100 nm: intermediate matrix diffusion length 100–150 nm: hydrodynamic and steric repulsion with tumor vessel, slower transvascular transport, low matrix diffusion length	<20 nm: poor internalization as aggregation needs to occur All sizes: matrix and tumor-associated macrophages sequester >88% of extravasated nanoparticles	[20a, 50, 54, 55]

with a low zeta potential than with high zeta potentials because the former avoids being trapped by the electrostatic bandpass formed by the extracellular matrix.[20b,50] Cationic nanomedicines are advantageous after extravasation into the tumor because they can act as adjuvants and trigger adsorption-mediated endocytosis by negatively-charged tumor cells and lysosomal escape at the target cell.[20b,45a,50,51]

The size of nanomedicine also significantly impacts biodistribution, circulation time, and tumor accumulation (**Table 2**). Nanoparticles with diameters below 200 nm are less likely to be cleared by the phagocytic cells of the reticuloendothelial system in the liver and spleen, although nanoparticles with diameters less than 20 nm can be more quickly cleared by renal excretion.[50] For example, the in vivo biodistribution of different nanoparticle species including lipid and polymeric nanoparticles across small (15–100 nm), medium (100–200 nm), and large (>200 nm) sizes over 2018 published datasets was analyzed by Kumar et al.[54] Despite different physicochemical properties, between 6 to 72 h post-injection, nanoparticles predominantly accumulated in the liver (18% of the injected dose g^{-1}), and spleen (12% of the injected dose g^{-1}) while nanoparticles accumulated significantly less in tumors (3% of the injected dose g^{-1}) and other tissues (<2% of the injected dose g^{-1}). For lipid nanoparticles, the small and medium nanoparticles had slower clearance and accumulated more in the liver, spleen, heart, intestine, and blood than large nanoparticles which undergo greater opsonization and phagocytosis. All polymeric nanoparticles had similar distributions in the liver, spleen, and bone at early time-points, while at ≈24 h the clearance of larger nanoparticles from the organs of the reticuloendothelial system was greater than small and medium nanoparticles. Additionally, small polymeric nanoparticles were distributed to the heart, intestine, kidney, and lung more than medium-sized nanoparticles.[54]

The hydrodynamic size of nanoparticles and their degree of aggregation have also been implicated in the degree of toxicity and hemolysis.[55] For example, the hemolysis of human whole blood in vitro was determined for silk- (zeta potential −14 mV), alginate- (zeta potential −27 mV) and gelatin-capped (zeta potential −10 mV) silver nanoparticles with hydrodynamic diameters of 79, 75, and 57 nm in blood plasma and compared to citrate-capped nanoparticles (82 nm, −26 mV). As the protein corona was similar for the biopolymer-capped nanoparticles by LC-MS/MS, hemolysis was determined to be size-dependent at doses above 100 µg mL^{-1}, with the smaller biopolymer-capped aggregates resulting in at least 1.5-fold increases to hemolysis compared to citrate-capped aggregates.[55] In contrast, preliminary biodistribution studies in BALB/c mice showed minimal hemolysis for the biopolymer-capped nanoparticles 8 days post-injection, while all nanoparticles accumulated mainly in the liver 24 h post-injection.[55]

Tumor penetration can be increased by reducing the nanomedicine's size to overcome the barriers to diffusion in the interstitial matrix. For example, the EPR effect is size-dependent due to the tumor vessel pore size (typically 40 to 200 nm).[50] Nanomedicines with diameters below 20 nm can undergo transvascular transport across normal vessels (pore sizes 6–12 nm), while nanomedicines ≈100–150 nm can be too large for complete tumor penetration due to hydrodynamic and steric repulsion with the pores of tumor vessels and poor diffusion through tumor tissue. Although smaller nanoparticles (<20 nm) more readily extravasate and penetrate the tumor,[50] they also have reduced drug-carrying capacity by either entrapment or surface adsorption. The nanoparticle surface area increases as the diameter decreases, thereby lowering the controlled-release properties of smaller nanoparticles. Further optimization of nanoparticle properties for tumor penetration may be accelerated by visualization of the nano-bio interactions occurring in the tumor microenvironment through real-time intravital microscopy and 3D in vitro tumor models.[10b]

The impact of the extracellular matrix on the diffusion characteristics of nanoparticles with different sizes, mechanical properties, and protein coronas was assessed by Dai et al.[20a] The authors used in vitro co-cultures of human ovarian SKOV-3 cancer cells and Raw264.7 murine macrophages in a 3D Matrigel-microchannel system to mimic the intra-tumoral microenvironment.[20a] At 24 h post-administration, 3% of the total cells were accessed by the 55 nm trastuzumab-coated gold nanoparticles. Uptake was more favorable by macrophages than cancer cells as 47% of the macrophage population interacted with the nanoparticles compared to 11% of nanoparticle-associated cancer cells. A smaller-sized nanoparticle of 15 nm was able to diffuse to a greater depth and interact with 8% of the total cells. Conversely, increasing the nanoparticle size to 100 nm resulted in no diffusion through the matrix or interaction with cells. The effect of nanoparticle hardness was investigated using 100 nm nanoparticles composed of different carrier materials (e.g., gold, silver, liposomes, and poly(lactic-*co*-glycolic acid)).[20a] Additionally, 55 nm gold nanoparticles were incubated with mouse serum to investigate the impact of the matrix on the diffusion of nanoparticles with and without a protein corona.[20a] Importantly, across a range of nanoparticles that differed in hardness and protein coronas, the matrix reduced the diffusion rate of

Table 3. The impact of nanoparticle morphology on biodistribution, tumor penetration, and internalization by cancer cells.

Biological impact			Refs.
Biodistribution	Tumor penetration	Cancer cell internalization	
Higher aspect ratio: lower reticuloendothelial system and mononuclear phagocyte system clearance, longer circulation times Discs: greater adhesion to endothelial cell walls than rods, ellipsoids, and hemispheres Prolate ellipsoid: greater cell attachment and lower phagocytosis rates than oblate ellipsoid and spheroid Higher specific surface area: faster degradation	Higher aspect ratio: greater margination to endothelial cells and target tumor	Spherical: contact angle-independent internalization Higher aspect ratio: optimal orientation for internalization when the major axis perpendicular to the cell membrane	[50, 57, 58]

all nanoparticles and resulted in less than 8% of the cancer cells being accessed. Next, the impact of the matrix density on the diffusion of 55 nm trastuzumab-coated gold nanoparticles was analyzed by increasing the Matrigel concentration, which resulted in a concentration-dependent reduction in diffusion distance and cell accessed. In this way, extracellular matrix degradation was reinforced as a treatment strategy.[20a]

The in vitro Matrigel experiments were reinforced in vivo by measuring the cell interaction with 15, 55, and 100 nm trastuzumab-coated gold nanoparticles at 24 h post injection to SKOV-3 xenograft tumor-bearing CD1 nude mice. Inductively coupled plasma-mass spectrometry revealed an average nanoparticle-to-tumor delivery efficiency for 55 nm particles of 0.59%, whereby flow cytometry indicated that only 0.001% of the injected dose interacted with SKOV-3 cancer cells. This meant that 9 per 1 million of the 55 nm nanoparticles were estimated to have reached the cancer cells due to the presence of intratumoral cellular (tumor-associated macrophages) and acellular (extracellular matrix) barriers. For example, the nanoparticles were 38 times more likely to interact and be phagocytosed by the perivascular tumor-associated macrophages than to interact with cancer cells. In total, the nanoparticles interacted with 2.4% of the cells in the tumor, as the remainder of the nanoparticles were trapped in the extracellular matrix. The smaller-sized nanoparticle of 15 nm resulted in a higher average delivery efficiency of 0.85% to the tumor, although only 0.0002% of the injected dose interacted with cancer cells as these smaller particles may need to be present at a high enough concentration to aggregate before uptake can occur. The authors suggested that the lower average nanoparticle-to-tumor delivery efficiency of the injected dose for 100 nm particles of 0.22% and the 0.001% nanoparticle-to-cancer delivery efficiency may be explained by their large size blocking diffusion through the extracellular matrix.[20a] For nanoparticles of all sizes, the extracellular matrix and tumor-associated macrophages sequestered more than 88% of extravasated nanoparticles.

4. Hierarchical Structure of Nanoparticles

The impacts of hierarchical structure and morphology on tumor uptake are poorly understood, as the effects are highly dependent on the tumor model and cell line.[10b] Morphology can affect the nanomedicine circulation time due to altered immune responses, endothelial cell adhesion, and flow behavior (**Table 3**).[56] The morphology dictates the curvature of the particles and whether phagocytosis will occur or whether cells will spread on the particle surface.[50] The internalization rate of spherical nanoparticles by macrophages does not depend on the contact angle with the cell, whereas nanoparticles with high-aspect ratios (e.g., rod-shaped) are optimally phagocytosed when the major axis lies perpendicular to the cell membrane, as wrapping of the nanoparticle requires less membrane reorganization.[50] High cell attachment rates can lead to spreading on the cell membrane and do not always translate into fast internalization. This was the case for prolate ellipsoid polystyrene nanoparticles (major axis 0.35–2.5 µm, minor axis 0.2–2.0 µm), which were found to have greater attachment but lower phagocytosis rates by murine RAW264.7 cells in vitro compared to spheroid (diameter 0.52–3.6 µm) and oblate ellipsoid particles (major axis 0.35–2.5 µm, minor axis 0.2–2.0 µm).[57]

Illustrating these concepts in vivo, the circulation time was longer for polymeric worm-like nanoparticles with aspect ratios greater than 20 than for spherical polymeric nanoparticles due to the decreased macrophage internalization of the worm-like nanoparticles.[56] Similarly, circulation times in rodent models were longer for cylindrical polymer micelles with lengths between 2 to 8 µm than for spherical micelles with diameters between 22 to 60 nm.[59] In vivo biodistribution studies in male Kunming mice with an orally administered spherical, long rod (aspect ratio 4) and short rod (aspect ratio 2) silica nanoparticles (diameters 150 nm) also confirmed that clearance by the reticuloendothelial system was lowest for nanoparticles with high aspect ratios.[58a] Combined with the greatest renal clearance for spherical nanoparticles, and short rods degrading the quickest in vitro due to their higher specific surface area (the ratio of surface area to volume), the longest circulation times were attained by long rods.[58a]

Other studies have suggested that longer circulation times of non-spherical nanoparticles can result from greater adhesion to the endothelial walls of blood vessels compared to spherical nanoparticles.[58b] Compared to the sequestered flow of spherical particles between red blood cells and vessel walls, the more complicated flow patterns in blood vessels for non-spherical nanoparticles can lead to their margination to the blood vessel walls.[56] The increased proximity to the endothelial walls can result in a greater affinity for endothelial cells by non-spherical nanomedicines than by spherical nanomedicines, with discs demonstrating greater margination and adhesion than rods, ellipsoids, and hemispheres.[58b]

Consequently, non-spherical nanoparticles can have a greater capacity for targeted delivery to endothelial cells[10b,58b] and a higher capacity for margination to the target tumor.[56] For example, the rate of tumor penetration was higher for polyethylene glycol–coated inorganic nanorods (15 × 54 nm) than for their nanosphere counterparts (35 nm), although both had similar hydrodynamic diameters between 30 to 40 nm and similar aqueous diffusion rates.[10b] However, the impact of morphology on the rate of internalization by cancer cells varies between studies and is dependent not only on the nanoparticle aspect ratios, but also on the target cell type, orientation of nanoparticles when binding to cell-membrane receptors, and nanoparticle flexibility.[50,60] The flexibility of the nanomedicine is dictated by the internal crystal structure, which has also been implicated in particle stability, payload release rate,[61] formation of the protein corona,[37,62] and clearance by the immune system.[56,63]

4.1. Surface Functionalization

Some improvements in cancer nanomedicines can arise by surface functionalization of the nanomedicines to engineer ligands for active targeting to tumor-expressed receptors or to apply stimulus-responsive stealth coatings that prevent undesired biological responses while the nanomedicine is in circulation.[14a]

In recent decades, several nanoimaging agents and nanomedicines have been engineered with active targeting or stimulus-responsiveness and are now clinically approved or entered into clinical trials and have shown improved tumor accumulation and reduced side effects.[64] Examples of actively targeted nanomedicines that have received clinical approval are antibody-drug conjugates, which consist of a monoclonal antibody designed to target a specific receptor overexpressed on the cancer cell surface and an antineoplastic agent conjugated through a non-cleavable (e.g., trastuzumab emtansine, brand name Kadcyla, which targets ErbB2 receptors) or a stimulus-responsive linker (e.g., sacituzumab govitecan, brand name Trodelvy, which targets human trophoblast cell-surface antigen Trop-2, Trastuzumab deruxtecan, brand name Enhertu, which targets ErbB2 receptors).[64b] Actively targeted nanoimaging agents are also available that incorporate mannose to target the CD-206 receptor on the surface of macrophages and these are used in the clinic for sentinel lymph node identification (e.g., technetium-99m-labelled, mannose-dextran conjugate branded as Lymphoseek).[64c,65]

However, at present, simple liposomal and micellar nanoformulations still predominate over actively targeting or stimulus-responsive nanoformulations in the group of >50 anticancer nanomedicines in current clinical trials.[14a,64b,66] The high failure rate associated with the translation of surface-functionalized nanomedicines from preclinical research to clinical approval is a consequence of many unsolved biological and technological issues, particularly the considerable work required to understand the nano-bio interactions that interfere with nanomedicine stability and biodistribution.[64b]

4.1.1. Active Targeting

Tumor cell uptake can be improved by active targeting through the decoration of nanomedicine surfaces with targeting ligands that bind specific endocytosis-prone receptors that are overexpressed on the surfaces of tumor cells. Active targeting is important for tissue accumulation in patients and for tumors in which the EPR effect is not the predominant mechanism of substance accumulation by the tumor. Improved drug delivery and efficacy over passively targeted controls has been achieved by targeting several cell membrane receptors, including the epidermal growth factor receptor (e.g., in mice bearing murine mammary carcinomas and mice bearing human cervical cancer and human colorectal cancer xenografts),[47a,67] the transferrin receptor (e.g., in mice bearing human prostate cancer and human colon adenocarcinoma xenografts),[68] integrins (e.g., in human mesenchymal stem cell lines),[10b,46,69] the folate receptor (e.g., in human breast adenocarcinoma cell lines),[70] and the asialoglycoprotein receptor (e.g., in human hepatoma patients).[71]

Dai et al. suggested that the reduction in tumor size and increased survival rate observed using actively targeted cancer nanomedicines in mouse models may reflect indiscriminate macrophage cytotoxicity and cell death.[20a] The authors used preclinical in vivo and in vitro mouse tumor models to quantify the active targeting efficiency, compared to passively targeted controls, of actively targeted trastuzumab-coated gold nanoparticles that target ErbB2 receptors and folate-coated gold nanoparticles which target folate receptors. The surface of the actively targeted gold nanoparticles was saturated with either PEG-conjugated trastuzumab or PEG-conjugated folate, and retrospectively functionalized with a mixture of Alexa Fluor 750-labeled 5 kDa PEG and methoxy-terminated 2 kDa PEG to reduce the protein corona. The passively targeted nanoparticles were functionalized with PEG but not with trastuzumab or folate, and the average hydrodynamic size of the passive control was ≈14 nm smaller than the trastuzumab-coated nanoparticles. The trastuzumab and passively targeted 55 nm gold nanoparticles were administered intravenously to preclinical human ovarian SKOV-3 xenograft mouse models with solid tumors, which are ErbB2 positive. At 24 h post injection, inductively coupled plasma-mass spectrometry revealed that the average nanoparticle-to-tumor delivery efficiency for actively targeted particles was 2.36 times greater than the 0.25% of the injected nanoparticle dose measured for passively targeted particles. However, flow cytometry with inductively coupled plasma-mass spectrometry also indicated that the average nanoparticle-to-cancer cell delivery efficiency of actively targeted nanoparticles (0.001%) was not significantly different to the passive control (0.003%). Conversely, the tumor-associated macrophages had accumulated 0.038% and 0.02% of the injected dose of actively and passively targeting nanoparticles respectively, which is ≈7–38 times the nanoparticle-to-cancer cell delivery efficiency. The remainder of the extravasated particles were in acellular regions. Likewise, the interactions of 100 and 140 nm trastuzumab-coated silica nanoparticles and their passively targeted controls with tumor-associated macrophages were found to be 2.7–31.9 times more likely than with cancer cells. Folate-coated nanoparticles and passively targeted controls were also produced with three different sizes of 15, 55, and 100 nm and were administered to a 4T1 orthotopic tumor model in BALB/c mice. Similarly to trastuzumab-coated nanoparticles, all sizes of folate-coated and control particles interacted preferentially with tumor-associated macrophages. Decoration with folate also did not significantly increase the nanoparticle-to-cancer cell delivery efficiency. Finally, the authors used in vitro co-culture SKOV-3 and Raw264.7 cell death experiments with 55 nm trastuzumab-doxorubicin-coated gold nanoparticles serving as an actively targeted nanomedicine model and doxorubicin-coated gold nanoparticles as the passively targeted control. Flow cytometry revealed that there was no significant difference in total cell death between active and passively targeted nanoparticle treatments, but only active targeting resulted in a significant, ninefold increase in cell death of macrophages than cancer cells. For active targeting, only macrophage cell death showed dose-dependence, whereas cancer cell death did not increase with nanoparticle dose. Nevertheless, active targeting was beneficial in vivo by reducing nanoparticle accumulation in the reticuloendothelial system organs.[20a]

The most common surface functionalization method involves targeting the tumor vasculature using the arginylglycylaspartic acid peptide. The peptide can bind to $\alpha v\beta 3$ integrin receptors that are not expressed in resting endothelial cells and some normal organ cells but are highly expressed on the surface of activated tumor endothelial cells, new vasculature, and some tumor cells.[10b,72] Targeting the tumor vasculature can enable the delivery of therapeutics that inhibit angiogenesis, thereby reducing tumor growth, promoting regression, and suppressing metastasis in mice in vivo. Surface modification with cyclic arginylglycylaspartic acid peptide has also significantly increased the tumor parenchyma-penetrating depth.[10b] Unfortunately, although the idea of active targeting was conceived many decades ago, only a few examples, such as Her2 targeted liposome (MM302), a targeted polymeric nanoparticle (BIND014), and targeted siRNA nanoparticle (CALAA-01), have reached the clinical trial stage.[10b] However, the growing pipeline of clinically approved antibody-drug conjugates is a clear testament that targeting is feasible in principle.

Most of the present understanding of nanomedicine–cell interactions has come from in vitro studies, which may not be accurate models for heterogeneous tumors in vivo. The relationship between the uptake mechanism and intracellular trafficking is also not linear, as many biochemical checkpoints determine the final nanoparticle destination.[37] Poor understanding of the in vivo uptake and trafficking mechanisms, along with patient-to-patient receptor expression heterogeneity, has contributed to the poor clinical performance of active versus passive anti-cancer nanomedicines.[73] High-resolution in vivo imaging may increase our understanding of the interactions occurring within the heterogeneous tumor microenvironment.[10b]

4.1.2. Stealth Coatings

Surface functionalization can also be used to engineer stealth nanoparticles by coating nanomedicines with hydrophilic, antifouling polymers, such as polyethylene glycol, and protein polymers, such as XTEN, or proline/alanine-rich sequences, which have the added benefit of greater biodegradability[74] (reviewed in ref. [75]). These stealth coatings limit immune clearance by reducing opsonization, although the coating also can lower cellular uptake by the target cells and subsequent endosomal escape compared to native nanomedicines, notably those with positive charges.[14a] Cleavable linkers have been tethered to the surface to theoretically ensure that the stealth coating remains intact during systemic circulation but will be selectively removed in the tumor microenvironment due to the low pH or enzyme activity. However, no self-adaptive nanomedicines have yet reached clinical trial status.[14a] Hence, the next sections of the review will cover current progress in anticancer silk nanomedicine methodology, including rational silk nanomedicine design that takes into account the physiological features of the tumor environment.

5. Silk Structure

Numerous insect species and arachnids produce silk proteins that have species-dependent amino acid primary sequences,[76] but all silk fibroins and spidroins are characterized by the presence of a block copolymer-like heavy chain,[77] which dictates many of the protein's properties (e.g., β-sheet crystallinity, high tensile strength, amphiphilicity, thermal stability). The territorial and cannibalistic nature of spiders prohibits their farming for silk production; therefore, spider silks (which are more correctly termed "spider silk-inspired proteins"), are typically manufactured using recombinant technologies. Supported by advances in protein expression systems, these exciting silks are now increasingly explored for biomedical applications, including nanomedicines and anticancer drug delivery (reviewed in ref. [78]). The first approval of this novel material class for human medical use is eagerly awaited. By contrast, the everyday silkworm (*Bombyx mori, B. mori*) silk, is already an approved silk (and the only one) for use in humans. Silk fibroin isolated from *B. mori* cocoons is particularly beneficial for nanomedicine applications, as the species can be farmed at scale and the silk has long since navigated the regulatory process.[79]

Mulberry silk from common *B. mori* is a well-characterized silk type that consists of a heavy (≈391 kDa) and a light (≈26 kDa) chain, linked by one disulfide bond at the heavy chain C-terminus (**Figure 3**).[80] In *B. mori* silk, the heavy chain has a block copolymer with a repeating amino acid sequence of 11 short hydrophilic regions and 12 hydrophobic blocks and nonrepetitive C- and N-termini. By contrast, the light chain has a nonrepeating amino acid sequence. The hydrophobic blocks make up 94% of the heavy chain and contain mostly glycine-X repeats, where X is alanine (A) (65%), serine (S) (23%), or tyrosine (Y) (9%).[80,81] The repetitive blocks can fold into anti-parallel β-sheet crystallites by forming hydrogen bonds, Van der Waals bonds, and hydrophobic interactions. The strength of the intermolecular bonds and the high density and degree of order within the β-sheet crystallites impart high mechanical strength.[82]

In the natural world, as the bave leaves the spinneret of the silkworm, the hydrophobic silk fibroin thread is coated with sericin, a protein that acts as a binding agent during cocoon spinning.[82,83] However, the silk fibroin and sericin mixture has been observed to induce an inflammatory response in humans;[84] therefore, the sericin must be removed by "degumming" the silk cocoons.[85] Isolating the silk fibroin protein from the spun cocoon has become the preferred method, as it offers a simpler extraction process compared to dissecting the silk gland.[86] Degumming methods include chemical, enzymatic, and physical processes that break down the sericin and cleave the intermolecular bonds that hold the fibroin and sericin together. The most well-used method involves boiling chopped silk cocoon pieces in an aqueous alka-

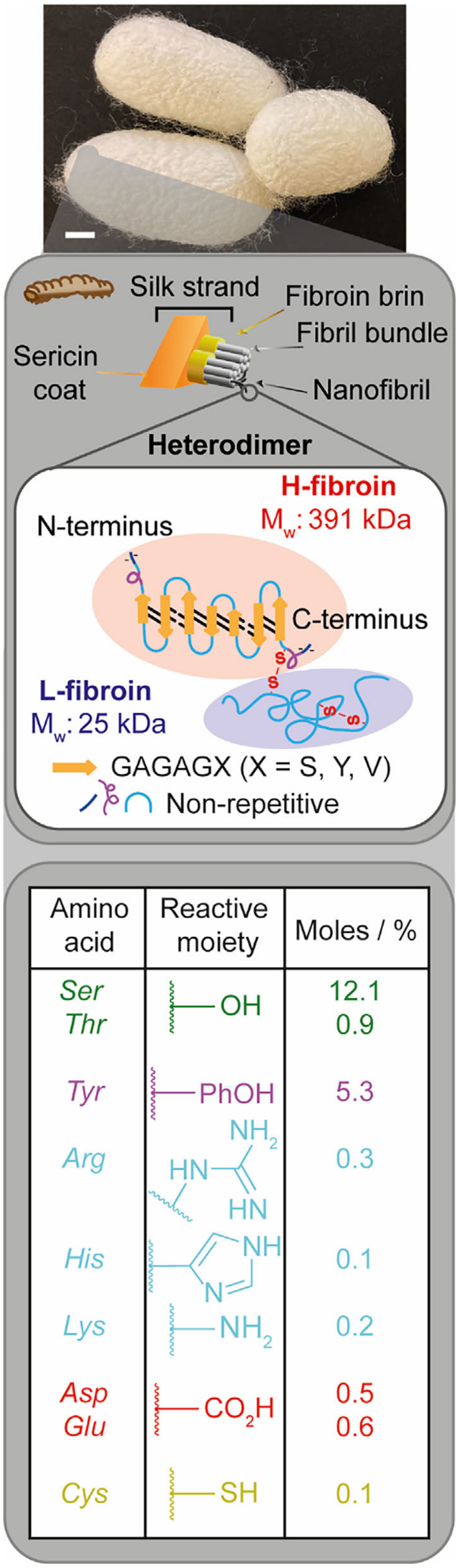

Amino acid	Reactive moiety	Moles / %
Ser Thr	OH	12.1 0.9
Tyr	PhOH	5.3
Arg	HN, NH$_2$, HN	0.3
His	NH, N	0.1
Lys	NH$_2$	0.2
Asp Glu	CO$_2$H	0.5 0.6
Cys	SH	0.1

Figure 3. Overview of the structure of *Bombyx mori* silk: From the amino acid composition to the cocoon. The scale bar is 0.5 cm in length. Image from.[81]

line solution.[86,87] These processes invariably cause chain scission of the fibroin protein backbone, resulting in a polydisperse mixture of silk fibroin polypeptides.[88]

The silk fibroin extracted by degumming is termed silk II and has a hydrophobic structure enriched with β-sheets.[82] The β-sheet crystallites and hierarchical structure of the silk fibers result in insolubility in water and most organic solvents,[81,86] which makes the silk obtained from degumming difficult to process into formats other than silk fabrics.[84] To dissolve the β-sheet crystals, hexafluoroisopropanol or saturated solutions of aqueous chaotropic agents (e.g., lithium bromide) at 60 °C are typically used in a process called regeneration.[86] The inputs of chemical and thermal energy act to break hydrogen and Van der Waals bonds in the silk II secondary structure to form a metastable, water-soluble silk I with a partially ordered structure and a higher percentage of α-helix and random coils (although the average molecular weight can also be reduced).[86,88b] The resulting aqueous liquid silk is typically dialyzed against water to remove chaotropic salts before further processing.

6. Silk as a Biomedical Material

For thousands of years, silk fibers have been processed into textiles and clothing. The silk spun by *B. mori* silkworms during their fifth instar is the market leader for silk goods due to its good mechanical properties and the ease with which silkworm breeding and silk cocoon collection can be scaled up and industrialized.[84]

B. mori silk has also been used clinically for several millennia in traditional healthcare.[79b,84] Since the discovery of the aseptic technique in the 1860s, sterile silk products have been used as a suture material[89] wound dressings, and reconstructive surgery support structures,[79b] due to their favorable biological properties, including biocompatibility, biodegradability, and handling.[79b,90] The complete removal of sericin from the silk fiber is important to ensure the non-immunogenicity of silk biomaterials, as residual sericin contamination is a reported potential cause of immune rejection responses.[79] Nevertheless, degummed *B. mori* silk has been approved as a biomaterial by the US Food and Drug Administration since 1993. In 2019, the first regenerated silk product, Silk Voice, a composite hyaluronic acid–silk microparticle hydrogel was clinically approved as a support structure to expedite vocal cord repair.[91]

Degummed and regenerated silk has many favorable properties, including the capacity to be processed into a variety of multiscale, hierarchical structures, such as films, scaffolds, hydrogels, microparticles, and nanoparticles.[79b,83] A variety of silk biomaterials have shown comparable in vitro cytocompatibility and in vivo biocompatibility with other biopolymers, such as collagen and polylactic acid.[79b] In addition, silk biomaterials processed into nanoparticles have shown biodegradability,[92] pH[93] and temperature[94] responsiveness, and stabilization of therapeutic payloads.[95]

Due to the presence of reactive amino acids (e.g., tyrosine and serine),[80,96] silk surfaces can also be decorated to improve their physiological responses. For example, silk nanoparticles can evade the mononuclear phagocyte system by bioconjugation to stealth polymers such as polyethylene glycol.[26b,97] Totten et al. demonstrated that in vitro TNF-α production by murine macrophages was significantly lower after incubation with polyethylene glycol-bound silk nanoparticles than with native silk nanoparticles.[26b]

The limitations of silk biomaterials arise due to the heterogeneity of the silk molecular structure within and between degummed and regenerated silk batches. This molecular structure heterogeneity occurs in part due to material aging.[98] However, a polydisperse mixture of silk molecules occurs due to the kinetically controlled amide backbone scission during processing,[88] which in turn can impact drug release performance.[99] With respect to the greenness of silk processing, silk sericulture, and cocoon acquisition are carbon sinks,[100] although standardization and scale-up of newer regeneration processes are still required to reduce the use of energy, water, and chemicals.[87,101] For example, a recent improvement to reduce the volume of water required for silk regeneration in the absence of additional pH-sensitive compounds has been to eliminate the dialysis of the chaotropic salt-liquid silk mixture before processing the liquid silk into silk nanoparticles.[102]

6.1. Silk and Silk-Inspired Proteins as Nanomedicines

Silk fibroin has generated considerable research interest as an alternative carrier material for nanomedicines due to its desirable properties,[78b,83] including the controllable physicochemical properties of the resultant silk nanoparticles.[103] For example, silk nanomedicines can be optimized for different modes of administration (e.g., intravitreal,[104] intravenous,[105] topical,[106] inhalation[107]) by changing the silk nanoparticle manufacturing process to tune the nanoparticle size, which can be varied between 40 nm to microns in diameter for spherical carriers.[106,108]To illustrate, using in vivo tumor models, silk nanoparticles between 100 and 20 nm were distributed to the tumor sites via intravenous administration.[105,109] Conversely, low-polydispersity silk nanoparticles with an average diameter of 42 nm were capable of in vivo transdermal delivery in rabbits by paracellular uptake through the stratum corneum to the dermis, a route not available to larger particles, which sequester in the stratum corneum.[106] Hence, drug adsorption to silk fibroin nanoparticle carriers with optimized critical quality attributes can improve the pharmacokinetic and pharmacodynamic properties of the payload.

The silk nanoparticle size can be tuned to alter drug adsorption, drug release, and cellular internalization. For example, reducing the nanoparticle size of silk nanoparticles manufactured by batch desolvation in acetone with in situ or post-synthetic drug loading improved the drug loading of doxorubicin from ≈1.0% for 130 nm particles to ≈0.9% for 65 nm.[110] In vitro drug release from smaller nanoparticles was also greater than for larger nanoparticles. Yet, in vitro intracellular uptake of the 65 nm nanoparticles by glioblastoma cells after a 4 h treatment was lower than the uptake of 130 nm nanoparticles in live and fixed cell imaging. Both nanoparticle sizes were trafficked to the lysosomes and cytosol, providing potential tools for cytosolic delivery.[110] The study reinforces the important balance between optimizing drug loading and understanding the trafficking pathways used for each nanoparticle to ensure payload delivery to the target organelles.

The morphology of silk nanomaterials can also be controlled by varying the manufacturing process, with examples ranging from spherical nanoparticles to rod-shaped microparticles and microcapsules,[95b,111] and nano- and microfibers.[112] Shimanovich et al. used emulsification in a microfluidic T-mixer and varied the silk feedstock viscosity and shear rate experienced within the channel to control microcapsule morphology.[95b] As the hierarchical structure of silk particles dictates their morphology, the increasing aspect ratio of silk microcapsules from spherical to thin and thick fibers was linked to the increasing intermolecular β-sheet crystallinity of the capsules' interior. Notably, the morphology did not impact the encapsulation efficiency of a fluorescent-labeled antibody (>95%) or small-molecules (>88%) but dictated the in vitro release kinetics. Thin continuous silk microfibers (0.5–2.5 µm) showed faster and greater overall release (>80%) of the fluorescent-labeled antibody in phosphate-buffered saline after 160 h compared to silk cylinders (5–35 µm × 4.5–65 µm), short (5–25 µm × 4.5–65 µm) microfibers and thick continuous (5–65 µm) microfibers (≈20%), while spherical (6–80 µm) silk microparticles had the poorest release (≈15%). The thin fibers also resulted in the fastest release of encapsulated glucose, tetracycline, and Remazol Brilliant Blue R, whereas thick fibers resulted in the slowest release kinetics. The release kinetics of cylinders, short fibers, and spheres were intermediate and varied with each small-molecule.[95b]

Surface potential is another key physicochemical property of silk nanoparticle carriers as it dictates the surface adsorption capability toward acids and bases. Silk fibroin nanoparticles have a net negative surface charge at physiological pH[93a,113] due to the silk pI of 4 to 5.[114] Molecular modeling experiments have indicated that the negative charge carried by silk fibroin at physiological pH is caused by the presence of ionizable groups, such as glutamic and aspartic acids,[115] which also make the silk nanoparticles pH-responsive.[93a] The surface electronegativity at physiological pH has been implicated in the lysosomotropic drug delivery[41] of silk nanoparticles verified by live cell confocal microscopy of MCF-7 cells[116] and monocytes.[117] Upon trafficking to the acidic lysosomes (≈pH 4.5), and to a lesser extent in the acidic tumor microenvironment (pH 6.5 to 6.9), the pH-responsiveness of the ionizable groups can trigger the release of surface-adsorbed drugs, an observation corroborated by in vitro drug release experiments with the weakly basic drug doxorubicin.[93,97,116] Doxorubicin release was further increased during carrier degradation, with a significantly increased release of doxorubicin observed at pH 4.5 in the presence of papain, a protease, which served as a model for lysosomal protein-degrading enzymes.[92] However, the surface electronegativity limits the loading of negatively charged small molecules and biologics (i.e., nucleic acids) and is expected to cause repulsion between the silk nanoparticle and the target cell membrane. However, uptake by the target tissue can be improved by functionalization of the silk nanoparticles using targeting and stealth ligands.

The conjugation of biologically active ligands improves silk nanomedicine efficacy by enabling receptor-mediated endocytosis and reducing reticuloendothelial system clearance.[78b,82] The chemically reactive amino acid groups in the silk fibroin protein sequence facilitate the chemical modification of amino acid side chains, enabling active targeting and stealth coating (**Table 4**). For example, bioconjugation of the arginylglycylaspartic acid se-

Table 4. Functionalized silk fibroin and silk-inspired particles as drug delivery vehicles.

Silk type/ Regeneration method	Production and functionalization methods	Payload (encapsulation efficiency/Drug loading)	Physicochemical properties (Size/PDI/Morphology/ Topography/Zeta potential)	Target (in vitro/in vivo model)	Results	Ref.
B. mori silk fibroin 0.02 м sodium carbonate (1 h) 9.3 м lithium bromide dissolution at 70 °C for 4 h	Carbodiimide coupling of silk fibroin solution with ethylenediamine Carbodiimide coupling with folic acid and fluorescein Self-assembly with chitosan-gold-doxorubicin nanoparticles	Doxorubicin (87.45% encapsulation efficiency)	Size 80 nm (FE-TEM)	Cervical cancer (human Hela in vitro)	Compared to uncoated controls: 1) Size and encapsulation efficiency increased from 8 nm and 70.83% 2) Reduced drug burst release due to diffusion barrier 3) Reduced cell viability and increased cellular uptake due to selective targeting	[118]
B. mori silk fibroin 0.02% w/v sodium carbonate (1 h) 9.3 м lithium bromide dissolution at 60 °C for 4 h	Desolvation in DMSO Post-synthetic drug loading Post-loading carbodiimide coupling with SP5-52 peptide	Gemcitabine (89% encapsulation efficiency/8.1% drug loading)	Size 302 nm (DLS) PDI 0.13 (DLS) Spherical (SEM) Zeta Potential -13 mV (ELS)	Lewis lung cancer (murine LL-2 in vitro and in vivo)	Compared to passively targeted controls: 1) Size increased from 156 nm and zeta potential increased from −37 mV 2) Improved cellular uptake and cancer cell viability reduced 3) Improved survival rate and metastasis	[119]
B. mori silk fibroin 0.02 м sodium carbonate 9.3 м lithium bromide dissolution at 60 °C for 4 h	Desolvation in acetone Post-synthetic drug loading Post-loading Tween-80 coating Post-coating radiolabeling with Technetium-99	Doxorubicin (85.1% encapsulation efficiency)	Size 116.5 nm (DLS) PDI 0.29 (DLS) Spherical (SEM) Zeta Potential −5.2 mV (ELS)	Gliobastoma (rat C-6, human LN-229 in vitro)	Compared to uncoated controls, Tween-80 coating: 1) Increased size from 92.8 nm, PDI from 0.159, and zeta potential from −6.56 mV. 2) Improved cellular uptake	[120]
B. mori silk fibroin 0.02 м sodium carbonate (0.5 h) 9.3 м lithium bromide dissolution at 70 °C for 2 h	Cellulose acetate blending with silk fibroin solution Addition of $HAuCl_4$, $AgNO_3$ and glutaraldehyde Electrospinning and in situ crosslinking	Au-Ag nanoparticles (17.32–53.21 nm)	Diameter 144.92 nm (FE-SEM) Nanofiber, rod (FE-SEM) Topography rough (AFM)	Breast cancer (human MCF-7 and MDA-MB-231 in vitro)	Compared to Au and Ag-nanofibers, the composite Au-Ag nanofiber: 1) Decreased diameter from 154.54 nm 2) Increased cell inhibition	[121]
B. mori silk fibroin 0.5% w/v sodium carbonate (0.33 h) × 3 Ajisawa's reagent at 78 °C for 2 h	Desolvation in acetone In situ drug loading Post-synthetic carbodiimide coupling with Lyp-1	Quercetin (50.3% encapsulation efficiency/5.61% drug loading)	Size 203.2 nm (DLS) PDI 0.11 (DLS) Spherical (TEM) Zeta potential −12.7 mV (ELS)	Triple-negative breast cancer (murine 4T1 in vitro and mice xenografts in vivo)	Compared to passively targeted controls: 1) Increased size, PDI, and zeta potential from 178.3 nm, 0.069 and − 15.3 mV 2) Increased internalization by 4T1 cells and mitochondrial damage in vitro 3) Increased tumor accumulation and reduction in tumor growth	[122]
B. mori silk fibroin 0.5% w/v sodium carbonate (0.33 h) × 3 Ajisawa's reagent at 78 °C for 2 h	Desolvation in acetone In situ drug loading Post-synthetic carbodiimide coupling with chondroitin sulfate	Curcumin (50.5% encapsulation efficiency/3.0% drug loading)	Size 175.4 nm (DLS) PDI 0.11 (DLS) Spherical (SEM and TEM) Zeta potential −35.5 mV (ELS)	Ulcerative colitis-colorectal cancer (murine 264.7 macrophages in vitro, Ulcerative colitis mice in vivo)	Non-cytotoxic in vivo Compared to passively targeted controls: 1) Increased size from 150.1 nm 2) Increased internalization by macrophages through CD44-mediated endocytosis 3) Increased accumulation in target tissue and improved bioavailability	[123]

(*Continued*)

Table 4. (Continued)

Silk type/ Regeneration method	Production and functionalization methods	Payload (encapsulation efficiency/Drug loading)	Physicochemical properties (Size/PDI/Morphology/ Topography/Zeta potential)	Target (in vitro/in vivo model)	Results	Ref.
B. mori silk fibroin 0.02 м sodium carbonate (1 h) × 2 9.2 м lithium bromide dissolution at 60 °C for 5 h	Calcium chloride-doxorubicin chelation in ethanol Addition of silk fibroin solution Nucleation of calcium carbonate clusters by ammonia and carbon dioxide diffusion	Doxorubicin (7.4% drug loading)	Size 198 nm (DLS) Spherical, monodisperse, mesoporous (SEM, TEM)	Triple-negative breast cancer (murine 4T1 in vitro and in vivo)	Increased tumor accumulation, tumor penetration, and antitumor immune response activated by low-intensity focused ultrasound Compared to uncoated nano-calcium carbonate reduced drug burst release due to diffusion barrier	[124]
B. mori silk fibroin 0.02 м sodium carbonate (0.5 h) 9.3 м lithium bromide dissolution at 60 °C for 4 h	Desolvation in acetone In situ drug loading Post-synthetic NHS-ester activated coupling with terminal alkyne linker Post-synthetic copper-catalyzed azide-alkyne cycloaddition with cylic-arginylglycyl-aspartic acid derivative	Curcumin (83.58% encapsulation efficiency/1.25% drug loading)	Size 142.7 nm (NTA) PDI 0.2 (DLS) Spherical (SEM) Zeta potential −23.7 mV (ELS)	Colorectal cancer (human CACO-2 in vitro), Cervical cancer (human Hela in vitro), Urinary bladder cancer (human ECV in vitro)	Compared to passively targeted controls: 1) Increased size from 128.9 nm and zeta potential decrease from −17.97 mV 2) Increased internalization by cells overexpressing integrin receptors 3) Reduced cell metabolic activity above 0.01 mg mL^{-1} (not dose-dependent)	[125]
B. mori silk fibroin 0.01 м sodium carbonate (1 h) + 0.003 м sodium carbonate (1 h) 9.3 м lithium bromide dissolution at 65 °C for 4 h	Methacrylation of silk fibroin solution Self-assembly and molecular imprinting with the print molecule (human serum albumin) Post-synthetic photo-crosslinking	-	Size 52.8–94.6 nm (DLS) PDI 0.13–0.35 (DLS) Irregular morphologies (SEM)	Human serum albumin for stealth capability and delivery to solid tumors (murine NIH/3T3 in vitro)	Non-cytotoxic at 1.5 mg mL^{-1} Compared to non-imprinted controls, selective and specific binding to human serum albumin with nanomolar affinity	[126]
B. mori silk fibroin 0.02 м sodium carbonate (0.5 h) 9.3 м lithium bromide dissolution at 60 °C for 2 h	Potassium phosphate salting out In situ drug loading Post-synthetic folic acid carbodiimide coupling and PEI grafting Post-synthetic drug loading	Doxorubicin (1.96–3.07% drug loading)	Size > 531.17 nm (DLS) Spherical (SEM) Mesoporous pore size ≈17.84 nm (nitrogen adsorption) Zeta potential +31.5 mV (ELS)	Cervical cancer (human Hela in vitro)	Compared to passively targeted controls: 1) Increased surface charge from −39.1 mV 2) Improved cellular uptake and cancer cell viability reduced	[127]
Bioengineered *Nephila clavipes* spider silk Expression from transformed *Esicherea coli (E. coli)* and thermal method purification	Genetic modification with H2.1 Her2-binding peptide Potassium phosphate salting out Post-synthetic drug loading	Doxorubicin (33.89% drug loading)	Size 357 nm (SEM) Spherical (SEM)	Breast cancer (murine D2F2/LUC and D2F2E2/LUC in vitro/murine D2F2E2/LUC tumor in vivo)	Compared to passively targeted controls: 1) Reduced particle size from 365 nm 2) Improved cellular binding and reduced cancer cell viability 3) Improved tumor delivery and tumor growth reduced	[78b, 128]
B. mori silk fibroin 0.02 м sodium carbonate (0.5 h) 9.3 м lithium bromide dissolution	Genipin crosslinking of silk fibroin solution Spray-freeze-drying In situ drug loading	Cisplatin (0.05% drug loading)	Size 10.08 µm (SEM) Porous, aggregated (SEM) Topography rough > 420.81 nm (AFM)	Non-small cell lung cancer (human A549 in vitro)	Compared to uncrosslinked controls: 1) Reduced particle size from 22.75 µm, increased porosity, increased aggregation 2) Increased cytotoxicity 3) Greater drug release	[107]

quence, folate, and the H2.1 Her2-binding peptide to silk fibroin particles improves their adhesion to cancer cells that overexpress integrins, folate receptors, and Her2 receptors, respectively (reviewed in refs. [78b, 82]). Folate conjugation can also aid the cellular uptake by folate-responsive cancer cells.[82] Alternatively, stealth coating nanoparticles by post-synthetic conjugation of polyethylene glycol can stabilize colloidal silk drug carriers in physiological model solutions,[97] improve the in vitro drug release of doxorubicin at pH 4.5,[97] reduce in vitro coagulation and platelet activation in human whole blood,[117] and alter the macrophage response.[26b] Consequently, the progression of silk nanomedicines to the clinic will require leverage of these conjugation techniques.

6.2. Silk Nanoparticle Manufacture

Processing liquid silk feeds for clinical development requires the development of manufacturing methodologies that are scalable, safe, low cost, sustainable, and reproducible between batches.[79b,81] In conjunction, the chemistry, manufacturing, controls, and good manufacturing practice requirements for nanomedicines increase in complexity as the technology moves from preclinical development to clinical development and then to commercialization, where standardized quality is essential.[129] The manufacture of simple nanoparticle systems, such as liposomes and polymeric nanoparticles, have been successfully scaled up using batch and continuous manufacturing unit operations, which are readily available or custom-designed in the pharmaceutical industry. However, complex nanoparticle systems that contain biological targeting ligands or biological components, carry a combination of therapeutics, use layer-by-layer assembly, or consist of composite materials can pose challenges to reproducible scale-up as they require multiple steps or sensitive components, and can require the modification of existing technology and the development of novel manufacturing processes.[10b] These limitations are particularly pertinent to silk fibroin, which is highly sensitive to processing conditions, such as pH, temperature, and chemical impurities, during degumming, dissolution, formulation, and purification.[130]

Moving from the lab scale to the clinical scale also typically requires rigorous screening of formulation factors or methods to ensure reproducible results. Consequently, designing nanoparticle manufacture methods at the lab scale that are amenable to scale-up is important. Although many lab-scale studies use bulk phase synthesis in semi-batch or batch formats, examples of methods that are amenable to scale-up to clinical development include non-wetting template technology,[131] coaxial turbulent jet mixer technology,[132] photolithography,[133] and microfluidic[134] technologies, which have the advantages of homogeneity, reproducibility, tunability, and high throughput (multiple kg day^{-1} can be produced). Optimizing formulation conditions at the lab scale and conducting early scale-up studies using these technologies can accelerate clinical translation.[10b]

The progression of some nanomedicines to the clinic have been complicated by a lack of standardized physicochemical and biological characterization, unreproducible formulation methods, insufficient characterization techniques, and insufficient comparisons between nanoparticle systems.[10b] The Minimum Information Reporting in Bio-Nano Experimental Literature guidelines have been proposed to increase the reproducibility of nanoformulation manufacturing details and characterization methodology.[135] Arguments against these one-size-fits-all rules are that they make characterization pipelines especially difficult for poorly funded research fields, early-stage researchers, and complex nanoparticle systems; therefore, they have not been universally accepted in the academic scientific literature.[136] Nevertheless, better standardization and clearer reporting of methods at the lab-scale would clearly be of long-term benefit to improve consistency across studies.

6.3. Silk Nanoparticle Formation in Batch Format

Considerable research interest has sparked in the use of silk nanoparticles as carriers of biologics and small molecule drugs, such as doxorubicin, which can be loaded during or after formulation (Table 4). For larger particles (0.2–10 μm), top–down methods such as jet milling,[137] bead milling,[138] and ball milling[139] provide simple approaches that are easy to scale up and do not require the use of (toxic) organic solvents.[140] However, the large sizes and wide polydispersity indexes of batch-produced particles, combined with the reduction in silk II content during grinding, means that these particles are more likely to be cytotoxic and have short circulation times.[140] Consequently, different bottom–up methods, namely instrumental-induced and chemical-induced methods, have been used to make silk nanoparticles in the bulk phase.

Instrumental-induced silk nanoparticle formation involves exposing a silk solution to physical forces, such as heat changes, pressure changes, electric fields, UV light, and shearing (**Table 5**).[130] Solution-enhanced dispersion by supercritical fluids processing exposes silk and a supercritical CO_2 solution to high pressure and temperature, which atomizes the solution into small droplets. With enhanced mixing, the droplets form nanoparticles after the CO_2 evaporates.[141] Silk particles may also be prepared by utilizing electric fields to ionize an aqueous silk solution. Here, the physicochemical properties of the resulting nanoparticles can be tuned by silk feed concentration and electric field voltage.[142] Electric fields formed by immersing conductive electrodes into a silk solution for a few minutes result in silk electric-gel formation at the positive electrode due to the local reduction in pH, which yields the constituent nanoparticles after freeze-drying.[143] Another method for fabricating nanoparticles uses shearing forces created by forcing silk through specially designed nozzles to tune particle properties with flow rate.[142,144] Electrospraying uses high voltage electric fields across a capillary nozzle to force the silk solution out as droplets, and the evaporation of water causes nanoprecipitation.[144] Spray-freeze-drying involves spraying a silk solution through an ultrasonic nozzle into liquid nitrogen, and the nanoparticles are then recovered by freeze-drying.[145] Laminar jet break-up involves breaking up the sprayed silk solution with a laminar jet and forming the silk II structure with methanol or water vapor.[145] The capillary-microdot method uses a microcapillary to distribute silk solution onto glass slides and subsequent freeze-drying to form the nanoparticles.[146] Finally, photolithography uses UV-induced protein crosslinking through a photomask of a specific pattern to

Table 5. Bottom–up production methods to fabricate silk nanoparticles. Adapted from references.[140,153]

	Method	Advantages	Disadvantages	Sizes/Payloads (Refs.)
Chemical	Salting out	Tunable physicochemical properties Tunable secondary structure Simple process No organic solvent Simple scale-up Mild conditions	Challenging to load hydrophobic and pH-sensitive payloads High polydispersity index Complex purification from salt-out agents	0.486–2.0 µm Alcian blue Rhodamine B Crystal Violet Doxorubicin[103,153,154]
	Desolvation	Tunable physicochemical properties Simple process Simple scale-up Mild conditions	Difficult to produce nanoparticles >200 nm Complex purification from organic solvents Challenging to load hydrophobic payloads Low drug loading capacity	35–300 nm Alpha mangostin Doxorubicin[93a,147,155]
	Polymer blending	Tunable physicochemical properties Tunable secondary structure Simple process Simple scale-up Mild conditions No organic solvent	Challenging to load hydrophobic payloads Complex purification from polymer residues Silk I secondary structure mainly produced	0.3–100 µm Bovine serum albumin Dextran Rhodamine B[111,149b]
	Self-assembly	Tunable physicochemical properties Tunable morphology Tunable secondary structure Mild conditions	Complex process Low throughput	0.02–6 µm Linalyl acetate Plasmid DNA[148]
	Reverse microemulsion	Simple process Tunable physicochemical properties	Complex purification from organic solvents and surfactants	167–169 nm Rhodamine B[151]
	Emulsion solvent evaporation	Simple process Mild conditions	Microparticles produced Complex purification from organic solvents	80–150 µm Bovine serum albumin[156]
	Emulsification diffusion	Simple scale-up Simple process Mild conditions	Microparticles produced Complex purification from organic solvents Silk I secondary structure mainly produced	60–150 µm Metformin[152]
	Cross-linking reaction	Simple process Tunable physicochemical properties	Complex purification from crosslinker reagents	0.3–1 µm Alpha mangostin[147]
Instrumental	Supercritical fluid solution	No organic solvent Simple scale-up High drug loading capacity	Expensive Complex process Silk I secondary structure mainly produced	28–194 nm Curcumin Indocyanine green[141a,157]
	Electrospraying	No organic solvent Tunable physicochemical properties High drug loading capacity	Expensive Silk I secondary structure mainly produced	59–75 nm Cisplatin[144]
	Electric field	No organic solvent Tunable physicochemical properties	Silk I secondary structure mainly produced	0.2–3.0 µm Bovine serum albumin[143]
	Spray-freeze-drying	No organic solvent Tunable physicochemical properties High drug loading capacity Cost effective	Microparticles produced Complex process Silk I secondary structure mainly produced Challenging to load hydrophobic and pH-sensitive payloads	3–20 µm Cisplatin[107]
	Laminar jet break-up	No organic solvent Mild conditions High drug loading capacity	Silk I secondary structure mainly produced Microparticles produced	100–440 µm Salicylic acid Propranolol Insulin-like growth Factor[145]
	Capillary-microdot printing	Tunable physicochemical properties	Complex purification from organic solvent Complex scale-up Low yield Silk I secondary structure mainly produced	20–140 nm Curcumin[146]
	Photolithography	No organic solvent Monodisperse size and morphology High throughput	Microparticles produced Not applicable for payloads sensitive to UV exposure	5–100 µm[133]

obtain microparticles, which are then recovered by washing with water.[133]

Chemical-induced silk nanoparticle formation requires the addition of other chemicals to a silk solution to induce covalent chemical or intermolecular bonding to expedite the silk I to silk II secondary structure transition, which occurs during nanoparticle formation (Table 5).[130] Cross-linking reactions introduce strong covalent bonds to initiate silk II formation by mixing silk with chemical crosslinkers, such as 1-ethyl-3-(3-dimethylaminopropyl)carbodiimide.[147] Self-assembly methods initiate protein–protein interactions by complex layer-by-layer silk deposition steps in the presence or absence of a particle template.[148] Polymer blending comprises four steps: air-drying of composite polymer-silk films or hydrogels for controlled silk self-assembly, dissolution of silk in water, sonication, and centrifugation to clean and concentrate the suspension.[127,149] The polymer blending technique has been used to optimize silk nanoparticle properties forming air-dried films from silk-poly vinyl alcohol blends and altering the processing parameters, such as the initial silk feed concentration, weight ratio of silk and polyvinyl alcohol, and sonication.[111,150] However, this method results in nanoparticles that are toxic and are predicted to possess an undesirable circulation time in clinical applications due to their high polydispersity index (0.40–0.68) and large nanoparticle size (ranging from 0.3–20 µm), as measured by dynamic light scattering (DLS).[111,150] Other fabrication methods proceed via a water-in-oil emulsion intermediate. For example, the reverse microemulsion technique involves mixing a silk solution into a surfactant-organic solvent mixture, such as Triton-X 100 and cyclohexane, which is then broken using an alcohol antisolvent, such as ethanol and methanol, to recover the nanoparticles.[151] Alternatively, emulsion solvent evaporation uses paraffin to generate a water-in-oil emulsion, which is then evaporated off by heating, leaving the aqueous nanoparticle suspension.[149a] Finally, emulsification diffusion homogenizes the silk solution with a water-immiscible organic solvent to form a water-in-oil emulsion, and the nanoparticles are purified by centrifugation.[152]

Simple coacervation is one of the most widely reported bulk phase methods in the literature and can be conducted by salting out or by desolvation with organic anti-solvents. Salting out involves increasing the ionic strength of an aqueous silk solution with a strong ionic solution, such as potassium phosphate, to pull out water from the silk hydration shell and facilitate protein–protein interactions.[127,153] Additionally, as the silk I to silk II transition occurs at around pH 5, acidic conditions result in the formation of silk II crystalline nanoparticles, whereas basic conditions result in nanoparticles rich in silk I.[103,153] The ability to tune secondary structure by varying pH, ionic strength, and silk feed concentration is useful for loading weakly basic drugs.[103,153] However, the nanoparticle sizes of 0.5–2.0 µm obtained by salting out, the <10% drug loading saturation, and the large batch-to-batch variability are not advantageous for anticancer applications.[103]

Organic anti-solvent desolvation is a popular formulation method as it is a simple one-step addition of aqueous liquid silk feed to a water-miscible organic anti-solvent, followed by purification of the silk nanoparticles from the cytotoxic anti-solvent (e.g., refs. [93a, 155]). The method utilizes the Marangoni effect[158] to govern the silk I to silk II transition and nanoparticle formation. Silk desolvation was first reported by Zhang et al. in 2007,[155b] whereby using at least 70% (v/v) of acetone resulted in low polydispersity index nanoparticles with sizes ranging between 35–125 nm as measured by transmission electron microscopy with a β-sheet crystalline silk II secondary structure measured by X-ray diffraction, FTIR and DSC. Zhang et al. tested polar protic solvents, including the first three monohydric alcohols, as well as polar aprotic solvents, including tetrahydrofuran and acetonitrile, but they reported that acetone gave the most favorable particle properties. This may be due to its intermediate polarity and shape, which enabled rapid transition of the α-helix to β-sheet secondary structure, as reducing the polarity of monohydric alcohols can increase the transition when added to silk films.[159] The reported silk nanoparticle production routes often use manual operations (e.g., refs. [93a, 155b]) that are susceptible to special-cause variations assignable to human error. For example, the dropping height and dropping rate are factors that are difficult to standardize using manual operations and can lead to unpredictable outcomes if not controlled as they affect mixing during desolvation. Thus to minimize special-cause variation and enhance mixing efficiency an effective and straightforward semi-batch approach at the laboratory scale was devised employing drop-by-drop nanoprecipitationy.[113a] Here, the impacts of varying the stirring rate and standing time on nanoparticle critical quality attributes, such as the particle size, surface charge, morphology, secondary structure, and yield, were analyzed. Both the initial dropping height (5.5 cm vs 7.5 cm) and stirring rate affected nanoparticle yield. However, the stirring rate was also a key factor influencing nanoparticle size (400 rpm < 200 rpm < 0 rpm). Charge and steric stabilizations created high energy barriers for nanoparticle growth because changes to the standing time of nanoparticles in the mother liquor for up to 24 h did not significantly impact their physicochemical properties.[113a] Next, silk nanoparticle morphology was tuned by controlling supersaturation and shear rate during nanoprecipitation using both semi-batch bulk mixing and micro-mixing (described below).[108] At flow rates below the critical shear rate for silk, increasing the silk concentration resulted in nanoparticles with smaller size, greater sphericity, and lower polydispersity index. Conversely, at flow rates exceedin the critical shear rate, increased supersaturation was counterbalanced by enhanced rates of shear-induced assembly.[108] Next, the scale-up of this semi-batch system was assessed. Silk precursor feeds processed in an unstirred semi-batch system (mixing time >120 s) significantly changed nanoparticle crystalline and physicochemical properties at the volumetric scale from 1.8 to 21.9 mL (i.e. 12-fold). However, the physicochemical properties remained stable after a further sixfold increase in scale to 138 mL. Greater reproducibility in nanoparticles properties was observed following a sixfold volumetric scale-up when combined with active stirring at 400 rpm that resulted in lower mixing times of similar duration. This indicated that both the average shear rate and bulk mixing time must be maintained during volumetric scale-up.[160] This 138 mL volumetric semi-batch system operating at a 29% yield supports a nanoparticle production rate of 0.53 g h^{-1} and 13 g per day.[160] This makes this system suitable for pre-clinical in vitro and in vivo studies.[132] Besides processing, the type of silk used during desolvation governs the resulting particle properties due to the different molecular structures. To illustrate, desolvation of silk extracted from *Antherea mylitta* cocoons with dimethyl sulfoxide resulted in nanoparticles ≈160 nm in size, compared to nanoparticle sizes of ≈180 nm obtained with silk extracted from *B. mori* cocoons.[161]

Recently, particles were generated in acetone by varying silk feed concentration between 5–10% w/v and varying the silk molecular weight. The silk molecular weight was varied by performing the degumming procedure for 1, 0.5, and 0.17 h to generate molecular weights of <71, 31–268, and 171–460 kDa.[110] Although the polydispersity index did not vary significantly, ranging between ≈0.20–0.32, increasing the silk feed molecular weight and silk feed concentration increased the nanoparticle size from 58 to 254 nm as measured by dynamic light scattering. Reducing the temperature to −20 °C generally resulted in the formation of smaller nanoparticles. Principal component analysis revealed a greater influence of the silk feed concentration than of the molecular weight of the silk feed on the particle diameter. Drawbacks to the desolvation method include the difficulty in tuning a nanoparticle size above 200 nm without knock-on increases to the polydispersity index and the need to purify the nanoparticle product from toxic antisolvents.[110]

The variety of bulk methods investigated is partly a consequence of the challenges that the silk feed polydispersity and self-assembly properties pose to reproducible manufacture. The inherent difficulty in achieving reproducible manufacture is exacerbated in batch format due to its time-dependent nature. This can lead to product property deviation throughout the formulation and can require long cleaning cycles to remove silk biofouling, which then lowers throughput. Consequently, optimizing silk formulation using continuous methodology has been proposed as a solution to increase the reproducibility and sustainability of silk nanoparticle manufacture.

6.4. Silk Nanoparticle Formation in Continuous Format

A need remains for the development and optimization of nanoformulation technology with increased scalability, reproducibility, and throughput to reduce production costs, safety concerns, and negative environmental impacts. Continuous production provides advantages over batch formats in terms of safety, cost, and environmental impact, as the production line is a one-step process that does not require interruptions by long emptying and cleaning cycles. Additionally, the reproducibility of product properties can be ensured as in-line monitoring systems can be designed to assure that the critical quality attributes of the products in the output stream are within the designated safe ranges, and production can be stopped should deviations occur. Chemical-induced silk nanoparticle formulation methods that can be translated into continuous format include desolvation,[113b,162] emulsification,[95b,163] and polymer blending.[164]

Microfluidic mixing is another pertinent production technology for continuous silk nanoparticle formulation as precise manipulation of process factors, including total flow rate and flow rate ratios, enables the control of particle properties.[165] Early microfluidic channel designs were made from polydimethylsiloxane using soft lithographic techniques. However, polydimethylsiloxane is incompatible with organic solvents, acids, and bases,[165,166] which can result in channel deformation and swelling during formulation and cleaning steps. Alternative materials, including glass, stainless steel, and polypropylene, improve the range of solvent compatibility but can be more expensive and difficult to produce.[165,166] Indeed, silk microfluidic devices have also been utilized for bio-microelectrical mechanical systems and chemical analysis applications and can be fabricated by micromolding on polydimethylsiloxane reverse molds[167] and by lithium bromide etching.[168] To address the challenge of biofouling and channel failure during formulation, channel surfaces can be treated with proteins and polymers to reduce surface adsorption.

The use of microfluidic devices may increase the rate of translation of nanoparticles from bench to clinic by improving production reproducibility and rate. For example, compared to bulk mixing with a mixing time on the order of seconds, the laminar flow fluid dynamics in the specialized mixing chambers are controllable and can be tuned to give mixing times on the order of microseconds to milliseconds.[169] When the mixing time is greater than the time required for nucleation and growth of the amphiphile chains, self-assembly occurs in a heterogeneous solvent mixture, leading to large aggregates and polydisperse nanoparticles. Conversely, when the mixing time is lower than the time required for nucleation and growth of the amphiphile chains, self-assembly occurs in a homogeneous mixed solvent resulting in smaller, monodisperse nanoparticles. Consequently, careful mixing chamber design can improve the consistency of nanoparticle critical quality attributes within and between batches.[169] The high total flow rates that can be achieved with microfluidics, combined with reduced cleaning cycles compared to bulk mixing, can also lead to greater, commercially relevant throughput.

The mixing chamber design should take into consideration the formation mechanism to ensure that fluid dynamics and mixing times produce a narrow distribution of nanoparticle properties without aggregation.[170] The control over silk nanoparticle formation has been improved by commonly used microfluidic designs, including staggered herringbone,[113b,162a] swirl,[162b] hydrodynamic flow-focusing,[164,171] double-junction,[172] and T-mixers.[95b] For example, the microfluidic T-mixer proved advantageous over batch emulsification for improving control over nano-microparticle size (51–2500 nm)[163] and microcapsule morphology (6–80 µm spheres to 5–35 µm × 4.5–65 µm rods).[95b] The use of a co-focusing mixer for polymer blending silk and polyvinyl alcohol (2.8–6.8 µm) resulted in a monodisperse microparticle size distribution (6.6 µm, polydispersity index 0.13) compared to batch format (5.8 µm, polydispersity index 0.65).[164] However, the double-junction, flow-focusing, and T-mixer require a low flow rate (µL h^{-1}) which make them unsuitable for high throughput (kg day^{-1}) commercial production.

The commercially relevant NanoAssemblr system uses a staggered herringbone mixer to provide advantages over batch format including low millisecond mixing times, high total flow rates of 12 mL min^{-1}, and full scalability to commercial formulation systems operating under current good manufacturing practice conditions.[173] Silk desolvation performed by Wongpinyochit et al.[113b] in the NanoAssemblr using *B. mori* silk degummed using the sodium carbonate method for 1 h with isopropanol and acetone antisolvents achieved physiologically relevant nanoparticles (110 to 310 nm) with low polydispersity (0.1 to 0.25), negative surface potential (−20 to −30 mV), and a silk II structure (48–

51% β-sheet content). The authors found that increasing the antisolvent: silk flow rate ratio from 1:1 to 5:1 increased the magnitude of the negative surface charge, decreased the size, decreased the size distribution, increased the colloidal stability over 42 days at 4 °C, and increased the yield. Scanning electron microscopy showed that increasing the total flow rate from 1 to 12 mL min^{-1} generally increased the presence of aggregates. The nanoparticles were not cytotoxic to a murine macrophage RAW 264.7 cell line with an IC$_{50}$ above 100 mg mL^{-1} and were trafficked to the lysosomes after 3 h.[113b]

Solomun et al.[162a] expanded upon this work by comparing the desolvation of sodium carbonate degummed *B. mori* silk with isopropanol in manual semi-batch format with the microfluidic NanoAssemblr system. The optimal microfluidic process factors of a 5:1 flow rate ratio and a 1 mL min^{-1} flow rate were set to optimize the silk degumming time.[162a] As in previous work,[113b] the nanoparticles showed good biocompatibility in RAW 264.7 cells with an IC$_{50}$ over 250 µg mL^{-1}.[162a] The authors found that 1 and 1.5 h degummed silk in microfluidic and semi-batch formats resulted in similar nanoparticle sizes (101–114 nm) and size distributions (0.088–0.107). The surface potential was significantly reduced in microfluidic manufacture (−28–(−29) mV) compared to semi-batch format (−39–(−43) mV). In both manual and microfluidic formats, increasing degumming time from 10 min to 1 and 1.5 h decreased the nanoparticle size and size distribution while the yield increased from 8% to ≈20%.[162a] Although the low volumetric throughput of optimal formulation (1 mL min^{-1}) and low yields[113b,162a] are key disadvantages of desolvation using the staggered herringbone mixer, operating microfluidic channels in parallel provides a solution to increase throughput for larger scale production. This approach is viable because microfluidic manufacturing demonstrated high repeatability between batches and reproducibility between microfluidic chips and participants.[160] Using this microfluidic format with 10 parallelized chips would generate silk nanoparticles at a rate of 0.43 g h^{-1} and 10 g per day, assuming a 14% yield. These amounts are adequate for preclinical in vitro and in vivo studies. However, this production rate is considerably lower than the kilograms per day required for clinical and industrial manufacture.[160] Therefore, more work is needed to scale these systems further.

To address low volumetric throughput, microfluidic swirl mixers have recently (2022) been used to manufacture silk nanoparticles by desolvation with ethanol at high flow rates (10–50 mL min^{-1}) with good reproducibility and low distribution of nanoparticle size. Nanoparticle purification was achieved with tangential flow filtration,[150] which provides a scalable technique to remove organic solvent and unbound payloads.[174] The nanoparticle properties were varied with total flow rate, silk feed concentration, and the number of mixing elements.[150] The authors used nanoparticle tracking analysis to measure the average nanoparticle size. The nanoparticle tracking results are similar to measurements obtained by DLS, but the single particle analysis gives a greater accuracy size distribution, as small nanoparticles in a polydisperse sample are not underestimated.[175] The authors used *B. mori* silk degummed using the sodium carbonate method for 30 min and found that the nanoparticle size and size distribution decreased as the total flow rate increased from 10 to 50 mL min^{-1}, with spherical morphologies for nanoparticles of sizes below 200 nm produced at 20 mL min^{-1} observed by transmission electron microscopy.[150] Increasing the number of mixing elements from one to four resulted in larger nanoparticles at each flow rate. Increasing the silk feed concentration from 0.5 to 3% w/v increased the nanoparticle size across all flow rates and from ≈100 to 300 nm at 10 mL min^{-1}. The maximum negative surface potential of the nanoparticles was −28 mV and the negative surface potential increased in magnitude with mixing elements. The negative surface charge, in conjunction with all nanoparticles bearing a silk II structure by FTIR analysis, resulted in colloidal stability when stored in water at 4 °C for 30 days. Although the authors did not report the nanoparticle yield, the swirl mixer proved advantageous over the standard T-mixer as smaller nanoparticles with narrower size distribution were produced when compared to using the same processing parameters.[150]

6.5. Synthetic Modification of Silk Nanomedicines

Silk fibroin has several chemically reactive amino acid groups that can be leveraged for homogeneous or heterogeneous bioconjugation (Figure 3). Functionalized silk nanoparticles for improved drug delivery by active targeting are listed (Table 4).[82,176] Chemical modification can be performed using the reactivity of natural amino acids in the silk protein chain, although these routes are typically associated with low chemoselectivity, multiple reaction steps, and low yields due to complicated purification. Carbodiimide, NHS-ester, and diazonium coupling have been popular methods for the functionalization of silk fibroin through silk primary amines or carboxylic acid side chains (**Figure 4**).

Homogeneous reactions, which are conducted in the solution-phase, are advantageous for the functionalization of silk substrates as they enable the downstream processing of liquid silk into different morphologies and material formats. For example, to improve anticancer efficacy by folate-mediated targeting, Horo et al.[118] functionalized silk using homogeneous carbodiimide coupling to first increase the amine content with ethylenediamine before performing coupling reactions with NHS ester-activated folate. The functionalized silk was purified of small molecule side products and unreacted reagents by dialysis and then processed using layer-by-layer deposition to form a coating for chitosan-gold microparticles.[118] The functionalized silk was analyzed by FTIR to determine a 14% conjugation efficiency of ethylenediamine and by UV–vis spectroscopy to determine an 18% conjugation efficiency of folate. Compared to the uncoated particles, the silk-folate coating resulted in decreased burst drug release, as it served as a diffusion barrier to encapsulated doxorubicin and increased the in vitro cytotoxicity in HeLa cell lines.[118] However, homogeneous reactions can suffer limitations due to the amphipathic nature of silk fibroin. For example, due to the low solubility of silk fibroin in organic solvents, many reactions are conducted in aqueous media. Consequently, the non-polar regions of the silk molecule form non-covalent interactions and undergo folding, which can protect reactive amino acids from incoming reactants, resulting in low reaction yields and complicated purifications to separate the product from unreacted substrates.

Heterogeneous chemical modification can involve the functionalization of silk fibroin nanoparticles, fibers, or films with

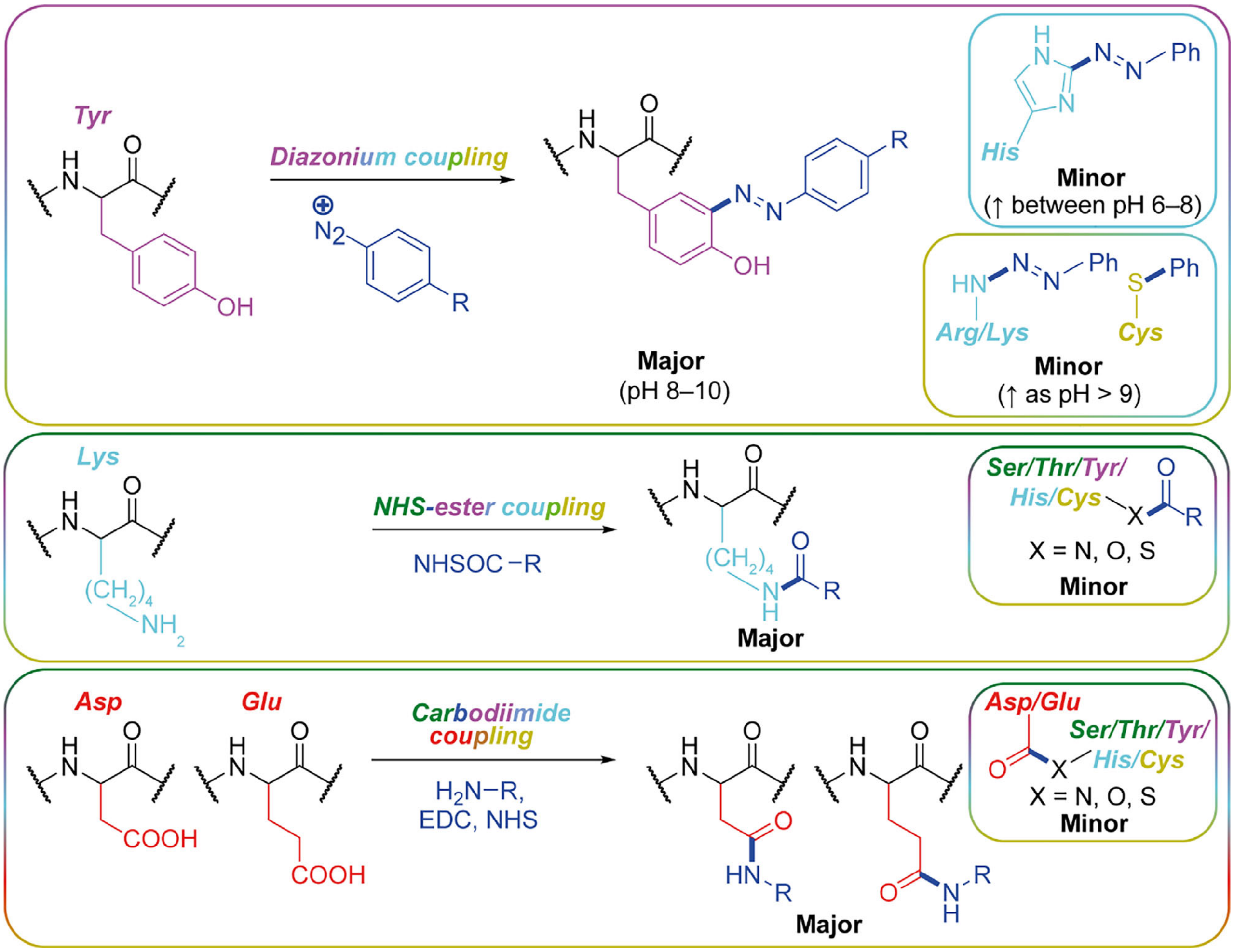

Figure 4. Strategies, which have a range of chemoselectivities, to functionalize the natural amino acids of silk fibroin. Image from.[81]

stealth ligands such as polyethylene glycol[26b,97] or biologically active molecules like RGD[73,125] folate,[70b,127] and targeting peptides[119] for active targeting. Compared to homogeneous modification, direct chemical modification of the material surface can make purification simpler, increase surface decoration, improve performance characteristics, and provide new functionalities to well-studied materials.[80,81,96] Indeed, Subia et al.[70b] reported the first chemically functionalized silk nanoparticles for active targeting using heterogeneous synthesis with acetone-desolvated *A. mylitta* silk nanoparticles (≈200 nm). The authors used carbodiimide coupling chemistry to produce *A. mylitta* silk-folate nanoparticles. Carbodiimide coupling can result in a low extent of modification due to the low carboxylic acid and primary amine content of silk in conjunction with the heterogeneous distribution of these residues along the protein sequence. Notably, the authors did not quantify the conjugation efficiency, although the functionalized nanoparticles were stable, spherical, and showed significantly greater endocytosis by human MDA-MB-231 triple-negative breast cancer cells compared to native silk nanoparticles. Folic acid competition studies indicated that the nanoparticles were recognized by the folate receptor, as endocytosis was blocked in the presence of excess folic acid.[70b] The authors loaded the folate-silk nanoparticles post-synthetically with doxorubicin,[70b] but drug loading could also be conducted in situ.[67a] For example, in situ paclitaxel loading during ethanol desolvation of 0.5% w/v silk fibroin was reported to give 10% w/w drug loading. The resulting silk-paclitaxel nanoparticles could undergo heterogeneous carbodiimide coupling with an anti-EGFR-iRGD dual-functional peptide and exceeded 75% conjugation efficiency, as measured using fluorescence spectroscopy. The peptide association with epidermal growth factor receptors and $\alpha v\beta 3/\alpha v\beta 5$ integrins increased the in vitro and in vivo anticancer efficacy compared to native silk controls. Additionally, the in vivo tumor targeting was greater compared to the silk controls, as determined by near infrared fluorescence imaging at 12 to 72 h after injection into HeLa-bearing mice. However, receptor engagement in vivo was not confirmed with soluble paclitaxel negative controls or soluble targeting residue competition studies.[67a] Important limitations to heterogeneous synthesis post-drug loading include the heightened complexity of purification, the possibility of side-reactivity with the payload, and the reduction to drug loads during purification.

In situ, drug loading during nanoparticle formation may increase drug encapsulation and stabilization compared to post-synthetic loading, which may ameliorate the side reactivity and desorption of drugs associated with the functionalization of loaded nanoparticles. Indeed, Shaidani et al. discovered that carbodiimide coupling of anti-EGFR with in situ doxorubicin-loaded silk-ethylenediamine nanoparticles resulted in no significant difference between nanoparticle-associated doxorubicin fluorescence before or after conjugation.[110] However, an indirect fluorescent antibody assay demonstrated that conjugation efficiency was greater for unloaded than loaded silk-ethylenediamine nanoparticles,[110] suggesting that post-loading strategies should first take into account the altered protein folding and surface amino acid distribution that can occur by drug encapsulation.

Diazonium coupling chemistry with silk fibroin produces an azobenzene derivative through an electrophilic aromatic substitution between a diazonium salt with silk tyrosine side chains (Figure 4). Diazonium coupling reactions have been used to alter the polarity of the silk molecule by functionalization with a range of moieties such as sulfonic acids, carboxylic acids, ketones, and alkanes.[80,81] The reaction is advantageous over other tyrosine functionalization methods for numerous reasons: it is conducted in mild, basic borate buffer (pH 9.0) in which silk fibroin is stable, readily available aniline derivatives can be used, electron-withdrawing and electron-donating anilines are tolerated, the reaction proceeds rapidly and can be quenched in 5–30 min, homogeneous and heterogeneous functionalization are possible, the installation of the azobenzene group can be monitored by ^{1}H-NMR or UV–vis spectroscopy at 325 nm, and the functionalized silk can be recovered by size exclusion chromatography or centrifugation. The reaction has tunable levels of modification by changing the ratio of diazonium salt to tyrosine or by changing the silk concentration. For example, the conversion efficiency can be maximized to ≈70% tyrosine conversion with dilute silk solutions and 0.9 equivalents of aniline derivatives containing electron-withdrawing substituents.[80,81] However, the reaction conjugation efficiency can be impeded to ≈20% by using aniline derivatives with electron-donating substituents or by low aqueous solubility of the diazonium salts. The drawbacks of the reaction include side reactions with histidine residues and silk gelation when conducted at high silk concentrations or when using an aniline derivative with hydrophobic substituents.[80,81]

One method to increase conjugation efficiency is to use reactions with low chemoselectivity, such as glutaraldehyde crosslinking. Silk nanoparticles (40–120 nm) assembled using acetone desolvation have been used as a carrier for long-acting insulin formulations by surface functionalization with insulin. Silk-insulin crosslinks were established using 0.7% glutaraldehyde for 8 h, the particles purified using repeated centrifugation, and ELISA used to demonstrate 90 to 115% recovery of insulin.[177] Conjugation of insulin to the silk nanoparticles resulted in greater stability of insulin in human serum and trypsin solution in vitro. The disadvantages of glutaraldehyde cross-linking include the denaturant properties of glutaraldehyde on proteins,[177] the low chemoselectivity resulting in undesired properties of the conjugate, and the high energy required to break strong covalent bonds for payload release.

Chemoselective silk bioconjugation can be achieved using enzymatic catalysts, such as horse-radish peroxidase[178] and N-acetylgalactosamine transferase,[179] which act on natural amino acids. Enzymatic catalysis presents a biorthogonal synthesis route, as the reactions are performed under physiological conditions, are highly site-selective, and can increase reaction yields while avoiding the need for co-factors or toxic metal catalysts. However, purification from residual enzymes can be a challenge, especially during reactions that induce gelation, as the enzymes can become incorporated into the hydrogel network.[178]

Bioorthogonal click chemistry has the advantage of being efficient in aqueous media and highly specific, enabling greater control over reaction outcomes, product purification, and product analysis. However, click chemistry can only be conducted with silk proteins following the chemical installation of a click handle.[180] For example, Scheibel and colleagues manufactured first-generation spider silk-inspired proteins using carbodiimide coupling with azidopropylamine. However, a limitation of the azide-alkyne cycloaddition for biomedical applications is the requirement for a toxic copper catalyst.[181] Hence, second-generation silks were developed by Scheibel and colleagues for thiol-ene click chemistry. The N-terminal end of a spider silk-inspired protein was genetically modified by the insertion of a short amino acid tag containing one cysteine and *E. coli* was used for heterologous production of the recombinant protein. The coupling efficiency of the recombinant protein with fluorescein-maleimide was assessed as 70–90%.[182] The exposed cysteines can then undergo thiol-maleimide Michael addition with maleimide-functionalized reactants. The limitations of these second-generation silks include the low degree of functionalization arising from the installation of one reactive cysteine per molecule and the lability of cysteine-maleimide conjugates to exchange reactions, which raises concerns regarding conjugate stability in vivo. Consequently, third-generation silks were designed to ensure protein expression with a biorthogonal non-canonical amino acid tag. Site-specific functionalization can be conducted using these recombinant[183] or in vivo spun silks in one-step using biorthogonal click chemistry without the requirement for enzymatic catalysts.[184] These systems use heterogeneous strain-promoted azide-alkyne cycloaddition which are copper-free click reactions. By reducing the number of reaction steps required for the installation of the desired functionality, third-generation silks can provide important advantages over their earlier counterparts, including reduced purification cost and increased product yield of functionalized silks. Overall, using click-capable recombinant silks as a substrate shortens synthetic routes and can simplify the purification of novel silk-based materials with improved properties.

7. Outlook and Summary

Silk continues to amaze as this biological material conquers novel healthcare applications. The emergence of silk-based nanomedicines is exciting but also demands a balanced approach to implement lessons learned while nurturing an orthogonal approach to tackle hard and unresolved challenges within cancer therapies and beyond. The adoption of continuous technology such as microfluidic mixing, tangential flow filtration technology, and in-line monitoring systems which can operate at commercially relevant throughputs, maintain sterile conditions, and can be appropriately scaled according to GMP manufacture will likely expedite the clinical journey of silk nanomedicines. To improve the scalability of manufacture and increase the yield of current production methods, the mechanism of silk nanoparticle formation should be considered while exploring the parameter space. Such exploration of the production parameter space has generated non-spherical morphologies and elucidated the dependence of model drug release kinetics with microcapsule morphology. In situ drug loading and formation of silk nanoparticles has proved advantageous over post-synthetic loading by shortening the formulation route: increasing throughput and decreasing the opportunity for contamination of sterile conditions. Promising improvements to the encapsulation and stabilization of drugs during post-loading functionalization have also already been reported for in situ doxorubicin loading. Functionalization of the natural amino acids in the silk protein using homogeneous and heterogeneous modification has led to the installation of stealth coatings and active targeting ligands and improved nanoparticle interactions with the target cells in vitro and in vivo. As discussed here, the adoption of recombinant silks and biocompatible click chemistry lowers the complexity of functionalization by enabling site-specific modification. Further exploration of recombinant silks will require increasing the number of click handles throughout the silk molecule for greater degrees of functionalization, and the introduction of multiple functionalities for improved biocompatibility and drug loading. Finally, future optimization of silk particle systems will require an increased understanding of their interaction with the tumor microenvironment using 3D in vitro tumor models and high-resolution in vivo imaging. The rise of nanomedicines and the realization of both opportunities and pitfalls must come to the fore to ensure that these silk nanomedicines have a bright future.

Acknowledgements

S.A.L.M. and F.P.S. acknowledge funding by Medical Research Scotland (PhD-1292-2018) and the Engineering and Physical Sciences Research Council (EPSRC) EP/V034995/1 to establish the Thermal Equipment Suite. This work was supported by the Fraunhofer Internal Programs under Grant No. Attract 40–04900 and the Carl-Zeiss-Stiftung zur Berufung internationaler Wissenschaftler:innen.

Conflict of Interest

The authors declare no conflict of interest.

Keywords

drug delivery, fibroin, nanomedicine, pharmaceutics, silk

Received: March 26, 2024
Revised: July 7, 2024
Published online: October 30, 2024

---

[1] E. Drexler, C. Peterson, G. Pergamit, *Nanomedicine*, William Morrow and Company Inc., New York **1991**.
[2] P. Iqbal, J. A. Preece, P. M. Mendes, in *Supramolecular Chemistry: From Molecules to Nanomaterials*, (Eds: J. W. Steed, P. A. Gale), Vol. *8*, John Wiley & Sons, Ltd., Oxford, UK **2012**, 1.
[3] a) R. Duncan, R. Gaspar, *Mol. Pharm.* **2011**, *8*, 2101; b) R. Duncan, S. C. Richardson, *Mol. Pharm.* **2012**, *9*, 2380; c) European Science Foundation Policy Briefing, **2005**, *23*, 1.
[4] a) D. Bobo, K. J. Robinson, J. Islam, K. J. Thurecht, S. R. Corrie, *Pharm. Res.* **2016**, *33*, 2373; b) G. Sahay, D. Y. Alakhova, A. V. Kabanov, *J. Controlled Release* **2010**, *145*, 182.
[5] J. Wahlich, A. Desai, F. Greco, K. Hill, A. T. Jones, R. J. Mrsny, G. Pasut, Y. Perrie, F. P. Seib, L. W. Seymour, I. F. Uchegbu, *Pharmaceutics* **2019**, *11*, 210.
[6] Y. Jia, Y. Jiang, Y. He, W. Zhang, J. Zou, K. T. Magar, H. Boucetta, C. Teng, W. He, *Pharmaceutics* **2022**, *15*, 774.
[7] a) Y. Barenholz, *J. Controlled Release* **2012**, *160*, 117; b) T. Lammers, M. Ferrari, *Nano Today* **2020**, *31*, 100853; c) E. Miele, G. P. Spinelli, E. Miele, F. Tomao, S. Tomao, *Int. J. Nanomed.* **2009**, *4*, 99; d) R. van der Meel, E. Sulheim, Y. Shi, F. Kiessling, W. J. M. Mulder, T. Lammers, *Nat. Nanotechnol.* **2019**, *14*, 1007.
[8] a) P. Decuzzi, D. Peer, D. D. Mascolo, A. L. Palange, P. N. Manghnani, S. M. Moghimi, Z. S. Farhangrazi, K. A. Howard, D. Rosenblum, T. Liang, Z. Chen, Z. Wang, J. J. Zhu, Z. Gu, N. Korin, D. Letourneur, C. Chauvierre, R. van der Meel, F. Kiessling, T. Lammers, *Nanotechnology* **2021**, *32*, 012001; b) X. Gao, L. Guo, J. Li, H. E. Thu, Z. Hussain, *J. Controlled Release* **2018**, *292*, 29.
[9] a) R. Sharma, N. Mody, U. Agrawal, S. P. Vyas, *Mini Rev. Med. Chem.* **2017**, *17*, 1746; b) C. L. Ventola, *P T* **2017**, *42*, 742.
[10] a) F. Lovering, J. Bikker, C. Humblet, *J. Med. Chem.* **2009**, *52*, 6752; b) J. Shi, P. W. Kantoff, R. Wooster, O. C. Farokhzad, *Nat. Rev. Cancer* **2017**, *17*, 20.
[11] a) Y. Shi, R. van der Meel, X. Chen, T. Lammers, *Theranostics* **2020**, *10*, 7921; b) S. Sindhwani, A. M. Syed, J. Ngai, B. R. Kingston, L. Maiorino, J. Rothschild, P. MacMillan, Y. Zhang, N. U. Rajesh, T. Hoang, J. L. Y. Wu, S. Wilhelm, A. Zilman, S. Gadde, A. Sulaiman, B. Ouyang, Z. Lin, L. Wang, M. Egeblad, W. C. W. Chan, *Nat. Mater.* **2020**, *19*, 566.
[12] P. Ehrlich, *Brit. J. Med.* **1913**, *16*, 353.
[13] Y. Matsumura, H. Maeda, *Cancer Res.* **1986**, *46*, 6387.
[14] a) I. de Lazaro, D. J. Mooney, *Nat. Mater.* **2021**, *20*, 1469; b) A. A. Natfji, D. Ravishankar, H. M. I. Osborn, F. Greco, *J. Pharm. Sci.* **2017**, *106*, 3179.
[15] D. Farrell, K. Ptak, N. J. Panaro, P. Grodzinski, *Pharm. Res.* **2011**, *28*, 273.
[16] T. Lammers, F. Kiessling, M. Ashford, W. Hennink, D. Crommelin, G. Storm, *Nat. Rev. Mater.* **2016**, 1.
[17] S. E. McNeil, *Nat. Rev. Mater.* **2016**, *1*, 16073.
[18] N. R. Patel, B. S. Pattni, A. H. Abouzeid, V. P. Torchilin, *Adv. Drug Delivery Rev.* **2013**, *65*, 1748.
[19] T. Lammers, *Nat. Mater.* **2020**, *19*, 1257.
[20] a) Q. Dai, S. Wilhelm, D. Ding, A. M. Syed, S. Sindhwani, Y. Zhang, Y. Y. Chen, P. MacMillan, W. C. W. Chan, *ACS Nano* **2018**, *12*, 8423; b) Q. Sun, Z. Zhou, N. Qiu, Y. S, *Adv. Mater.* **2017**, *29*, 201606628; c) S. Wilhelm, A. J. Tavares, Q. Dai, S. Ohta, J. Audet, H. F. Dvorak, W. C. W. Chan, *Nat. Rev. Mater.* **2016**, *1*, 16014.
[21] K. J. Harrington, S. Mohammadtaghi, P. S. Uster, D. Glass, A. M. Peters, R. G. Vile, J. S. Stewart, *Clin. Cancer Res.* **2001**, *7*, 243.
[22] B. Ouyang, W. Poon, Y. N. Zhang, Z. P. Lin, B. R. Kingston, A. J. Tavares, Y. Zhang, J. Chen, M. S. Valic, A. M. Syed, P. MacMillan, J. Couture-Senecal, G. Zheng, W. C. W. Chan, *Nat. Mater.* **2020**, *19*, 1362.
[23] a) Y. Altay, S. Cao, H. Che, L. Abdelmohsen, J. C. M. van Hest, *Biomacromolecules* **2019**, *20*, 4053; b) W. J. Brownlee, F. P. Seib, *Sci. Rep.* **2018**, *8*, 12318.
[24] M. A. Miller, Y. R. Zheng, S. Gadde, C. Pfirschke, H. Zope, C. Engblom, R. H. Kohler, Y. Iwamoto, K. S. Yang, B. Askevold, N. Kolishetti, M. Pittet, S. J. Lippard, O. C. Farokhzad, R. Weissleder, *Nat. Commun.* **2015**, *6*, 8692.
[25] D. Alizadeh, L. Zhang, J. Hwang, T. Schluep, B. Badie, *Nanomedicine* **2010**, *6*, 382.
[26] a) R. Saborano, T. Wongpinyochit, J. D. Totten, B. F. Johnston, F. P. Seib, I. F. Duarte, *Adv. Healthcare Mater.* **2017**, *6*, 1601240; b) J. D.

Totten, T. Wongpinyochit, J. Carrola, I. F. Duarte, F. P. Seib, *ACS Appl. Mater. Interfaces* **2019**, *11*, 14515.
[27] L. N. M. Nguyen, W. Ngo, Z. P. Lin, S. Sindhwani, P. MacMillan, S. M. Mladjenovic, W. C. W. Chan, *Nat. Rev. Bioeng.* **2024**, *2*, 201.
[28] G. Griffiths, J. Gruenberg, M. Marsh, J. Wohlmann, A. T. Jones, R. G. Parton, *Adv. Drug Delivery Rev.* **2022**, *188*, 114403.
[29] H. Appelqvist, P. Waster, K. Kagedal, K. Ollinger, *J. Mol. Cell Biol.* **2013**, *5*, 214.
[30] C. De Duve, B. C. Pressman, R. Gianetto, R. Wattiaux, F. Appelmans, *Biochem. J.* **1955**, *60*, 604.
[31] a) C. de Duve, *Nat. Cell Biol.* **2005**, *7*, 847; b) M. Hu, J. Chen, S. Liu, H. Xu, *Autophagy* **2023**, *19*, 1368.
[32] J. J. Rennick, A. P. R. Johnston, R. G. Parton, *Nat. Nanotechnol.* **2021**, *16*, 266.
[33] V. T. Cong, J. L. Houng, M. Kavallaris, X. Chen, R. D. Tilley, J. J. Gooding, *Chem. Soc. Rev.* **2022**, *51*, 7531.
[34] I. Licona-Limon, C. A. Garay-Canales, O. Munoz-Paleta, E. Ortega, *J. Leukocyte Biol.* **2015**, *98*, 85.
[35] X. P. Lin, J. D. Mintern, P. A. Gleeson, *Membranes* **2020**, *10*, 177.
[36] J. P. Lim, P. A. Gleeson, *Immunol. Cell Biol.* **2011**, *89*, 836.
[37] Y. T. Ho, R. D. Kamm, J. C. Y. Kah, *Nanoscale* **2018**, *10*, 12386.
[38] a) S. Patel, J. Kim, M. Herrera, A. Mukherjee, A. V. Kabanov, G. Sahay, *Adv. Drug Delivery Rev.* **2019**, *144*, 90; b) S. Watanabe, E. Boucrot, *Curr. Opin. Cell Biol.* **2017**, *47*, 64.
[39] a) A. Trouet, D. Deprez-de Campeneere, C. De Duve, *Nat. New Biol.* **1972**, *239*, 110; b) A. Trouet, D. Deprez-de Campeneere, M. de Smedt-Malengreaux, G. Atassi, *Eur. J. Cancer* **1974**, *10*, 405.
[40] C. de Duve, T. de Barsy, B. Poole, A. Trouet, P. Tulkens, F. Van Hoof, *Biochem. Pharmacol.* **1974**, *23*, 2495.
[41] J. B. Lloyd, *Adv. Drug Delivery Rev.* **2000**, *41*, 189.
[42] M. Srinivasarao, C. V. Galliford, P. S. Low, *Nat. Rev. Drug Discovery* **2015**, *14*, 203.
[43] J. L. Markman, A. Rekechenetskiy, E. Holler, J. Y. Ljubimova, *Adv. Drug Delivery Rev.* **2013**, *65*, 1866.
[44] A. L. B. Seynhaeve, B. M. Dicheva, S. Hoving, G. A. Koning, T. L. M. Ten Hagen, *J. Controlled Release* **2013**, *172*, 330.
[45] a) A. Ahmad, J. M. Khan, S. Haque, *Biochimie* **2019**, *160*, 61; b) L. I. Selby, C. M. Cortez-Jugo, G. K. Such, A. P. R. Johnston, *Wiley Interdiscip. Rev.: Nanomed. Nanobiotechnol.* **2017**, *9*, e1452.
[46] T. Cohen-Karni, K. J. Jeong, J. H. Tsui, G. Reznor, M. Mustata, M. Wanunu, A. Graham, C. Marks, D. C. Bell, R. Langer, D. S. Kohane, *Nano Lett.* **2012**, *12*, 5403.
[47] a) H. Lee, A. F. Shields, B. A. Siegel, K. D. Miller, I. Krop, C. X. Ma, P. M. LoRusso, P. N. Munster, K. Campbell, D. F. Gaddy, S. C. Leonard, E. Geretti, S. J. Blocker, D. B. Kirpotin, V. Moyo, T. J. Wickham, B. S. Hendriks, *Clin. Cancer Res.* **2017**, *23*, 4190; b) M. Overchuk, G. Zheng, *Biomaterials* **2018**, *156*, 217.
[48] M. R. Choi, K. J. Stanton-Maxey, J. K. Stanley, C. S. Levin, R. Bardhan, D. Akin, S. Badve, J. Sturgis, J. P. Robinson, R. Bashir, N. J. Halas, S. E. Clare, *Nano Lett.* **2007**, *7*, 3759.
[49] M. R. Choi, R. Bardhan, K. J. Stanton-Maxey, S. Badve, H. Nakshatri, K. M. Stantz, N. Cao, N. J. Halas, S. E. Clare, *Cancer Nanotechnol.* **2012**, *3*, 47.
[50] R. Zein, W. Sharrouf, K. Selting, *J. Oncol.* **2020**, *2020*, 5194780.
[51] S. Shah, N. Rangaraj, S. B. Singh, S. Srivastava, *Colloid Interface Sci. Commun.* **2021**, *42*, 100406.
[52] H. Ishiwata, N. Suzuki, S. Ando, H. Kikuchi, T. Kitagawa, *J. Controlled Release* **2000**, *69*, 139.
[53] a) M. Weiss, J. Fan, M. Claudel, T. Sonntag, P. Didier, C. Ronzani, L. Lebeau, F. Pons, *J. Nanobiotechnol.* **2021**, *19*, 5; b) T. Stylianopoulos, K. Soteriou, D. Fukumura, R. K. Jain, *Ann. Biomed. Eng.* **2013**, *41*, 68; c) T. S. Levchenko, R. Rammohan, A. N. Lukyanov, K. R. Whiteman, V. P. Torchilin, *Int. J. Pharm.* **2002**, *240*, 95.
[54] M. Kumar, P. Kulkarni, S. Liu, N. Chemuturi, D. K. Shah, *Adv. Drug Delivery Rev.* **2023**, *194*, 114708.
[55] P. Srivastava, C. Gunawan, A. Soeriyadi, R. Amal, K. Hoehn, C. Marquis, *Nanoscale Adv.* **2021**, *3*, 4424.
[56] P. Lagarrigue, F. Moncalvo, F. Cellesi, *Pharmaceutics* **2023**, *15*, 32.
[57] G. Sharma, D. T. Valenta, Y. Altman, S. Harvey, H. Xie, S. Mitragotri, J. W. Smith, *J. Controlled Release* **2010**, *147*, 408.
[58] a) Y. Zhao, Y. Wang, F. Ran, Y. Cui, C. Liu, Q. Zhao, Y. Gao, D. Wang, S. Wang, *Sci. Rep.* **2017**, *7*, 4131; b) J. T. Lovegrove, B. Kent, S. Forster, C. J. Garvey, M. H. Stenzel, *Exploration* **2023**, *3*, 20220075.
[59] Y. Geng, P. Dalhaimer, S. Cai, R. Tsai, M. Tewari, T. Minko, D. E. Discher, *Nat. Nanotechnol.* **2007**, *2*, 249.
[60] W. Zhanga, R. Taheri-Ledari, F. Ganjalib, S. S. Mirmohammadib, F. S. Qazib, M. Saeidiradb, A. KashtiArayb, S. Zarei-Shokatb, Y. Tianc, A. Maleki, *RSC Adv.* **2023**, *13*, 80.
[61] M. Souri, M. Soltani, F. Moradi Kashkooli, M. Kiani Shahvandi, M. Chiani, F. S. Shariati, M. R. Mehrabi, L. L. Munn, *Mater. Today Bio* **2022**, *13*, 100208.
[62] a) G. Caracciolo, *Nanoscale* **2018**, *10*, 4167; b) V. H. Nguyen, B. J. Lee, *Int. J. Nanomed.* **2017**, *12*, 3137.
[63] Y. Hui, X. Yi, D. Wibowo, G. Yang, A. P. J. Middelberg, H. Gao, C. X. Zhao, *Sci. Adv.* **2020**, *6*, eaaz4316.
[64] a) B. Bortot, A. Mangogna, G. Di Lorenzo, G. Stabile, G. Ricci, S. Biffi, *J. Nanobiotechnol.* **2023**, *21*, 155; b) A. I. Fraguas-Sanchez, I. Lozza, A. I. Torres-Suarez, *Cancers* **2022**, *14*, 1198; c) J. I. Hare, T. Lammers, M. B. Ashford, S. Puri, G. Storm, S. T. Barry, *Adv. Drug Delivery Rev.* **2017**, *108*, 25.
[65] a) S. P. Leong, *Clin. Exp. Metastasis* **2022**, *39*, 39; b) V. K. Sondak, D. W. King, J. S. Zager, S. Schneebaum, J. Kim, S. P. Leong, M. B. Faries, B. J. Averbook, S. R. Martinez, C. A. Puleo, J. L. Messina, L. Christman, A. M. Wallace, *Ann. Surg. Oncol.* **2013**, *20*, 680; c) A. M. Wallace, L. K. Han, S. P. Povoski, K. Deck, S. Schneebaum, N. C. Hall, C. K. Hoh, K. K. Limmer, H. Krontiras, T. G. Frazier, C. Cox, E. Avisar, M. Faries, D. W. King, L. Christman, D. R. Vera, *Ann. Surg. Oncol.* **2013**, *20*, 2590.
[66] D. Fan, Y. Cao, M. Cao, Y. Wang, Y. Cao, T. Gong, *Signal Transduction Targeted Ther.* **2023**, *8*, 293.
[67] a) X. Bian, P. Wu, H. Sha, H. Qian, Q. Wang, L. Cheng, Y. Yang, M. Yang, B. Liu, *OncoTargets Ther.* **2016**, *9*, 3153; b) Z. Ye, Y. Zhang, Y. Liu, Y. Liu, J. Tu, Y. Shen, *Int. J. Nanomed.* **2021**, *16*, 2443.
[68] a) T. R. Daniels, T. Delgado, G. Helguera, M. L. Penichet, *Clin. Immunol.* **2006**, *121*, 159; b) T. Lammers, W. E. Hennink, G. Storm, *Br. J. Cancer* **2008**, *99*, 392.
[69] J. Cui, K. Alt, Y. Ju, S. T. Gunawan, J. A. Braunger, T. Y. Wang, Y. Dai, Q. Dai, J. J. Richardson, J. Guo, M. Bjornmalm, C. E. Hagemeyer, F. Caruso, *Biomacromolecules* **2019**, *20*, 3592.
[70] a) S. Sabharanjak, S. Mayor, *Adv. Drug Delivery Rev.* **2004**, *56*, 1099; b) B. Subia, S. Chandra, S. Talukdar, S. C. Kundu, *Integr. Biol.* **2014**, *6*, 203.
[71] P. J. Julyan, L. W. Seymour, D. R. Ferry, S. Daryani, C. M. Boivin, J. Doran, M. David, D. Anderson, C. Christodoulou, A. M. Young, S. Hesslewood, D. J. Kerr, *J. Controlled Release* **1999**, *57*, 281.
[72] Z. Liu, F. Wang, X. Chen, *Drug Dev. Res.* **2008**, *69*, 329.
[73] B. Mao, C. Liu, W. Zheng, X. Li, R. Ge, H. Shen, X. Guo, Q. Lian, X. Shen, C. Li, *Biomaterials* **2018**, *161*, 306.
[74] V. Schellenberger, C. W. Wang, N. C. Geething, B. J. Spink, A. Campbell, W. To, M. D. Scholle, Y. Yin, Y. Yao, O. Bogin, J. L. Cleland, J. Silverman, W. P. Stemmer, *Nat. Biotechnol.* **2009**, *27*, 1186.
[75] R. Anand, J. Vallooran, in *Beyond polyethylene glycol*, (Ed: A. Parambath), Woodhead Publishing Series in Biomaterials, Cambridge, **2018**, pp. 299–315.
[76] S. C. Kundu, B. Kundu, S. Talukdar, S. Bano, S. Nayak, J. Kundu, B. B. Mandal, N. Bhardwaj, M. Botlagunta, B. C. Dash, C. Acharya, A. K. Ghosh, *Biopolymers* **2012**, *97*, 455.

[77] K. Arakawa, N. Kono, A. D. Malay, A. Tateishi, N. Ifuku, H. Masunaga, R. Sato, K. Tsuchiya, R. Ohtoshi, D. Pedrazzoli, A. Shinohara, Y. Ito, H. Nakamura, A. Tanikawa, Y. Suzuki, T. Ichikawa, S. Fujita, M. Fujiwara, M. Tomita, S. J. Blamires, J. A. Chuah, H. Craig, C. P. Foong, G. Greco, J. Guan, C. Holland, D. L. Kaplan, K. Sudesh, B. B. Mandal, Y. Norma-Rashid, et al., *Sci. Adv.* **2022**, *8*, eabo6043.

[78] a) T. B. Aigner, E. DeSimone, T. Scheibel, *Adv. Mater.* **2018**, *30*, 1704636; b) A. Florczak, I. Grzechowiak, T. Deptuch, K. Kucharczyk, A. Kaminska, H. Dams-Kozlowska, *Materials* **2020**, *13*, 4946.

[79] a) A. Bucciarelli, A. Motta, *Biomater. Adv.* **2022**, *139*, 212982; b) C. Holland, K. Numata, J. Rnjak-Kovacina, F. P. Seib, *Adv. Healthcare Mater.* **2019**, *8*, e1800465.

[80] A. R. Murphy, D. L. Kaplan, *J. Mater. Chem.* **2009**, *19*, 6443.

[81] S. A. L. Matthew, F. P. Seib, *ACS Biomater. Sci. Eng.* **2024**, *10*, 12.

[82] P. K. M. Rajendra, B. S. S. Nidamanuri, A. P. Balan, S. Venkatachalam, N. Jawahar, *J. Nanopart. Res.* **2022**, *24*, 141.

[83] F. P. Seib, *AIMS Bioeng.* **2017**, *4*, 239.

[84] X. Yao, S. Zou, S. Fan, Q. Niu, Y. Zhang, *Mater. Today Bio* **2022**, *16*, 100381.

[85] a) D. Ebrahimi, O. Tokareva, N. G. Rim, J. Y. Wong, D. L. Kaplan, M. J. Buehler, *ACS Biomater. Sci. Eng.* **2015**, *1*, 864; b) C. Vepari, D. L. Kaplan, *Prog. Polym. Sci.* **2007**, *32*, 991.

[86] D. N. Rockwood, R. C. Preda, T. Yucel, X. Wang, M. L. Lovett, D. L. Kaplan, *Nat. Protoc.* **2011**, *6*, 1612.

[87] M. K. DeBari, C. I. King, 3rd, T. A. Altgold, R. D. Abbott, *ACS Biomater. Sci. Eng.* **2021**, *7*, 3530.

[88] a) H. J. Kim, M. K. Kim, K. H. Lee, S. K. Nho, M. S. Han, I. C. Um, *Int. J. Biol. Macromol.* **2017**, *104*, 294; b) L. S. Wray, X. Hu, J. Gallego, I. Georgakoudi, F. G. Omenetto, D. Schmidt, D. L. Kaplan, *J. Biomed. Mater. Res., Part B* **2011**, *99*, 89.

[89] a) T. M. Muffly, A. P. Tizzano, M. D. Walters, *J. R. Soc. Med.* **2011**, *104*, 107; b) W. Thomson, *Dublin J. Med. Sci.* **1883**, *75*, 240.

[90] a) C. Guo, C. Li, D. L. Kaplan, *Biomacromolecules* **2020**, *21*, 1678; b) A. E. Thurber, F. G. Omenetto, D. L. Kaplan, *Biomaterials* **2015**, *71*, 145.

[91] J. E. Brown, C. P. Gulka, J. E. M. Giordano, M. P. Montero, A. Hoang, T. L. Carroll, *J. Voice* **2019**, *33*, 773.

[92] T. Wongpinyochit, B. F. Johnston, F. P. Seib, *ACS Biomater. Sci. Eng.* **2018**, *4*, 942.

[93] a) F. P. Seib, G. T. Jones, J. Rnjak-Kovacina, Y. Lin, D. L. Kaplan, *Adv. Healthcare Mater.* **2013**, *2*, 1606; b) T. Wongpinyochit, B. F. Johnston, F. P. Seib, *J. Vis. Exp.* **2016**.

[94] Q. Lu, H. Zhu, C. Zhang, F. Zhang, B. Zhang, D. L. Kaplan, *Biomacromolecules* **2012**, *13*, 826.

[95] a) A. B. Li, J. A. Kluge, N. A. Guziewicz, F. G. Omenetto, D. L. Kaplan, *J. Controlled Release* **2015**, *219*, 416; b) U. Shimanovich, F. S. Ruggeri, E. De Genst, J. Adamcik, T. P. Barros, D. Porter, T. Muller, R. Mezzenga, C. M. Dobson, F. Vollrath, C. Holland, T. P. J. Knowles, *Nat. Commun.* **2017**, *8*, 15902.

[96] J. Chen, H. Venkatesan, J. Hu, *Adv. Eng. Mater.* **2018**, *20*, 1700961.

[97] T. Wongpinyochit, P. Uhlmann, A. J. Urquhart, F. P. Seib, *Biomacromolecules* **2015**, *16*, 3712.

[98] S. M. V. Ramirez, *Beppu J. Mater. Res.* **2019**, *34*, 1944.

[99] E. M. Pritchard, X. Hu, V. Finley, C. K. Kuo, D. L. Kaplan, *Macromol. Biosci.* **2013**, *13*, 311.

[100] G. K. Rohela, P. Shukla, Muttanna, R. K., S. R. Chowdhury, *Trees For People* **2020**, *2*, 100011.

[101] L. Zhu, J. Lin, L. Pei, Y. Luo, D. Li, Z. Huang, *Polymers* **2022**, *14*, 659.

[102] A. J. Ruiz-Alcaraz, M. A. Nunez-Sanchez, M. A. Asensio Ruiz, M. A. Martinez-Sanchez, A. Oliva-Bolarin, T. Martinez Martinez, J. J. Perez Cuadrado, B. Ramos-Molina, A. A. Lozano-Perez, *Pharmaceutics* **2023**, *15*, 263.

[103] A. S. Lammel, X. Hu, S. H. Park, D. L. Kaplan, T. R. Scheibel, *Biomaterials* **2010**, *31*, 4583.

[104] P. Yang, Y. Dong, D. Huang, C. Zhu, H. Liu, X. Pan, C. Wu, *Pharm. Dev. Technol.* **2019**, *24*, 575.

[105] H. L. Xu, D. L. ZhuGe, P. P. Chen, M. Q. Tong, M. T. Lin, X. Jiang, Y. W. Zheng, B. Chen, X. K. Li, Y. Z. Zhao, *Drug Delivery* **2018**, *25*, 364.

[106] I. Takeuchi, Y. Shimamura, Y. Kakami, T. Kameda, K. Hattori, S. Miura, H. Shirai, M. Okumura, T. Inagi, H. Terada, K. Makino, *Colloids Surf. B Biointerfaces* **2019**, *175*, 564.

[107] S. Y. Kim, D. Naskar, S. C. Kundu, D. P. Bishop, P. A. Doble, A. V. Boddy, H. K. Chan, I. B. Wall, W. Chrzanowski, *Sci. Rep.* **2015**, *5*, 11878.

[108] S. A. L. Matthew, R. Rezwan, J. Kaewchuchuen, Y. Perrie, F. P. Seib, *RSC Adv.* **2022**, *12*, 7357.

[109] Y. Tian, X. Jiang, X. Chen, Z. Shao, W. Yang, *Adv. Mater.* **2014**, *26*, 7393.

[110] S. Shaidani, C. Jacobus, J. K. Sahoo, K. Harrington, H. Johnson, O. Foster, S. Cui, O. Hasturk, T. Falcucci, Y. Chen, M. Fletcher, C. Brooks, G. P. Holland, D. L. Kaplan, *ACS Appl. Nano Mater.* **2023**, *6*, 18967.

[111] X. Wang, T. Yucel, Q. Lu, X. Hu, D. L. Kaplan, *Biomaterials* **2010**, *31*, 1025.

[112] a) Y. Hu, J. Yu, L. Liu, Y. Fan, *J. Mater. Chem. B* **2019**, *7*, 1450; b) M. E. Kinahan, E. Filippidi, S. Koster, X. Hu, H. M. Evans, T. Pfohl, D. L. Kaplan, J. Wong, *Biomacromolecules* **2011**, *12*, 1504.

[113] a) S. A. L. Matthew, J. D. Totten, S. Phuagkhaopong, G. Egan, K. Witte, Y. Perrie, F. P. Seib, *ACS Biomater. Sci. Eng.* **2020**, *6*, 6748; b) T. Wongpinyochit, J. D. Totten, B. F. Johnston, F. P. Seib, *Nanoscale Adv.* **2019**, *1*, 873.

[114] F. P. Seib, M. F. Maitz, X. Hu, C. Werner, D. L. Kaplan, *Biomaterials* **2012**, *33*, 1017.

[115] T. Wongpinyochit, A. D. Vassileiou, S. Gupta, S. H. Mushrif, B. F. Johnston, F. P. Seib, *J. Phys. Chem. Lett.* **2019**, *10*, 4278.

[116] J. D. Totten, T. Wongpinyochit, F. P. Seib, *J. Drug Target* **2017**, *25*, 865.

[117] M. F. Maitz, C. Sperling, T. Wongpinyochit, M. Herklotz, C. Werner, F. P. Seib, *Nanomedicine* **2017**, *13*, 2633.

[118] H. Horo, S. Bhattacharyya, B. Mandal, L. M. Kundu, *Carbohydr. Polym.* **2021**, *258*, 117659.

[119] F. Mottaghitalab, M. Kiani, M. Farokhi, S. C. Kundu, R. L. Reis, M. Gholami, H. Bardania, R. Dinarvand, P. Geramifar, D. Beiki, F. Atyabi, *ACS Appl. Mater. Interfaces* **2017**, *9*, 31600.

[120] V. Pandey, T. Haider, A. R. Chandak, A. Chakraborty, S. Banerjee, V. Soni, *J. Drug Delivery Sci. Technol.* **2020**, *56*, 101539.

[121] M. Arumugam, B. Murugesan, N. Pandiyan, D. K. Chinnalagu, G. Rangasamy, S. Mahalingam, *Mater. Sci. Eng., C* **2021**, *123*, 112019.

[122] X. Zhang, Y. Huang, H. Song, B. S. B. Canup, S. Gou, Z. She, F. Dai, B. Ke, B. Xiao, *J. Controlled Release* **2020**, *328*, 454.

[123] S. Gou, Y. Huang, Y. Wan, Y. Ma, X. Zhou, X. Tong, J. Huang, Y. Kang, G. Pan, F. Dai, B. Xiao, *Biomaterials* **2019**, *212*, 39.

[124] M. Tan, Y. Chen, Y. Guo, C. Yang, M. Liu, D. Guo, Z. Wang, Y. Cao, H. Ran, *Biomater. Sci.* **2020**, *8*, 6703.

[125] E. Bari, M. Serra, M. Paolillo, E. Bernardi, S. Tengattini, F. Piccinini, C. Lanni, M. Sorlini, G. Bisbano, E. Calleri, M. L. Torre, S. Perteghella, *Cancers* **2021**, *13*, 1185.

[126] A. M. Bossi, A. Bucciarelli, D. Maniglio, *ACS Appl. Mater. Interfaces* **2021**, *13*, 31431.

[127] N. Sun, R. Lei, J. Xu, S. C. Kundu, Y. Cai, J. Yao, Q. Ni, *J. Mater. Sci.* **2019**, *54*, 3319.

[128] a) A. Florczak, A. Mackiewicz, H. Dams-Kozlowska, *Biomacromolecules* **2014**, *15*, 2971; b) A. Florczak, T. Deptuch, K. Kucharczyk, H. Dams-Kozlowska, *Cancers* **2021**, *13*, 5389.

[129] S. Dordevic, M. M. Gonzalez, I. Conejos-Sanchez, B. Carreira, S. Pozzi, R. C. Acurcio, R. Satchi-Fainaro, H. F. Florindo, M. J. Vicent, *Drug Delivery Transl. Res.* **2022**, *12*, 500.

[130] A. L. Martinez-Lopez, C. Pangua, C. Reboredo, R. Campion, J. Morales-Gracia, J. M. Irache, *Int. J. Pharm.* **2020**, *581*, 119289.

[131] J. Xu, D. H. Wong, J. D. Byrne, K. Chen, C. Bowerman, J. M. DeSimone, *Angew. Chem., Int. Ed.* **2013**, *52*, 6580.

[132] J. M. Lim, A. Swami, L. M. Gilson, S. Chopra, S. Choi, J. Wu, R. Langer, R. Karnik, O. C. Farokhzad, *ACS Nano* **2014**, *8*, 6056.

[133] R. K. Pal, N. E. Kurland, C. Jiang, S. C. Kundu, N. Zhang, V. K. Yadavalli, *Eur. Polym. J.* **2016**, *85*, 421.

[134] C. Webb, S. Ip, N. V. Bathula, P. Popova, S. K. V. Soriano, H. H. Ly, B. Eryilmaz, V. A. Nguyen Huu, R. Broadhead, M. Rabel, I. Villamagna, S. Abraham, V. Raeesi, A. Thomas, S. Clarke, E. C. Ramsay, Y. Perrie, A. K. Blakney, *Mol. Pharm.* **2022**, *19*, 1047.

[135] H. S. Leong, K. S. Butler, C. J. Brinker, M. Azzawi, S. Conlan, C. Dufes, A. Owen, S. Rannard, C. Scott, C. Chen, M. A. Dobrovolskaia, S. V. Kozlov, A. Prina-Mello, R. Schmid, P. Wick, F. Caputo, P. Boisseau, R. M. Crist, S. E. McNeil, B. Fadeel, L. Tran, S. F. Hansen, N. B. Hartmann, L. P. W. Clausen, L. M. Skjolding, A. Baun, M. Agerstrand, Z. Gu, D. A. Lamprou, C. Hoskins, et al., *Nat. Nanotechnol.* **2019**, *14*, 629.

[136] a) H. F. Florindo, A. Madi, R. Satchi-Fainaro, *Nat. Nanotechnol.* **2019**, *14*, 627; b) T. Lammers, G. Storm, *Nat. Nanotechnol.* **2019**, *14*, 626.

[137] M. Kazemimostaghim, R. Rajkhowa, X. Wang, *Powder Technol.* **2015**, *283*, 321.

[138] a) M. Kazemimostaghim, R. Rajkhowa, T. Tsuzuki, X. Wang, *Powder Technol.* **2013**, *241*, 230; b) M. Kazemimostaghim, R. Rajkhowa, X. Wang, *Powder Technol.* **2014**, *262*, 156.

[139] R. Rajkhowa, L. Wang, X. Wang, *Powder Technol.* **2008**, *185*, 87.

[140] D. T. Pham, W. Tiyaboonchai, *Drug Delivery* **2020**, *27*, 431.

[141] a) B. Q. Chen, R. K. Kankala, G. Y. He, D. Y. Yang, G. P. Li, P. Wang, S. B. Wang, Y. S. Zhang, A. Z. Chen, *ACS Biomater. Sci. Eng.* **2018**, *4*, 3487; b) R. K. Kankala, B. Q. Chen, C. G. Liu, H. X. Tang, S. B. Wang, A. Z. Chen, *Int. J. Nanomed.* **2018**, *13*, 4227; c) Z. Zhao, Y. Li, A. Z. Chen, Z. J. Zheng, J. Y. Hu, J. S. Li, G. Li, *Ind. Eng. Chem. Res.* **2013**, *52*, 3752.

[142] A. Gholami, H. Tavanai, A. R. Moradi, *J. Nanopart. Res.* **2011**, *13*, 2089.

[143] a) Q. Lu, Y. Huang, M. Li, B. Zuo, S. Lu, J. Wang, H. Zhu, D. L. Kaplan, *Acta Biomater.* **2011**, *7*, 2394; b) Y. Huang, Q. Lu, M. Li, B. Zhang, H. Zhu, *Sci. China Press* **2011**, *56*, 1013.

[144] J. Qu, Y. Liu, Y. Yu, J. Li, J. Luo, M. Li, *Mater. Sci. Eng., C* **2014**, *44*, 166.

[145] E. Wenk, A. J. Wandrey, H. P. Merkle, L. Meinel, *J. Controlled Release* **2008**, *132*, 26.

[146] V. Gupta, A. Aseh, C. N. Rios, B. B. Aggarwal, A. B. Mathur, *Int. J. Nanomed.* **2009**, *4*, 115.

[147] D. T. Pham, N. Saelim, W. Tiyaboonchai, *Colloids Surf. B Biointerfaces* **2019**, *181*, 705.

[148] a) S. Bai, S. Liu, C. Zhang, W. Xu, Q. Lu, H. Han, D. L. Kaplan, H. Zhu, *Acta Biomater.* **2013**, *9*, 7806; b) L. Li, S. Puhl, L. Meinel, O. Germershaus, *Biomaterials* **2014**, *35*, 7929; c) Y. Wang, Q. Cheng, J. Liu, Z. Tariq, Z. Zheng, G. Li, D. L. Kaplan, X. Wang, *ACS Biomater. Sci. Eng.* **2020**, *6*, 4583.

[149] a) X. Wang, E. Wenk, X. Hu, G. R. Castro, L. Meinel, X. Wang, C. Li, H. Merkle, D. L. Kaplan, *Biomaterials* **2007**, *28*, 4161; b) J. Wu, Z. Zheng, G. Li, D. L. Kaplan, X. Wang, *Acta Biomater.* **2016**, *39*, 156.

[150] M. A. Tomeh, R. Hadianamrei, D. Xu, S. Brown, X. Zhao, *Colloids Surf. B Biointerfaces* **2022**, *216*, 112549.

[151] S. J. Myung, H.-S. S. Kim, Y. Kim, P. Chen, H.-J. J. Jin, *Macromol. Res.* **2008**, *16*, 604.

[152] a) Q. Han, T. Zheng, L. Zhang, N. Wu, J. Liang, H. Wu, G. Li, *J. Biomater. Sci. Polym. Ed.* **2022**, *33*, 747; b) Y. Baimark, P. Srihanam, Y. Srisuwan, P. Phinyocheep, *J. Appl. Polym. Sci.* **2010**, *118*, 1127.

[153] K. DeFrates, T. Markiewicz, P. Gallo, A. Rack, A. Weyhmiller, B. Jarmusik, X. Hu, *Int. J. Mol. Sci.* **2018**, *19*, 1717.

[154] A. B. Mathur, V. Gupta, *Nanomedicine* **2010**, *5*, 807.

[155] a) A. S. Gobin, R. Rhea, R. A. Newman, A. B. Mathur, *Int. J. Nanomed.* **2006**, *1*, 81; b) Y. Q. Zhang, W. D. Shen, R. L. Xiang, L. J. Zhuge, W. J. Gao, W. B. Wang, *J. Nanopart. Res.* **2007**, *9*, 885; c) A. A. Lozano-Pérez, M. G. Montalbán, S. D. Aznar-Cervantes, F. Cragnolini, J. L. Cenis, G. Víllora, *J. Appl. Polym. Sci.* **2015**, *132*, 41702.

[156] Y. Srisuwan, P. Srihanam, Y. Baimark, *J. Macromol. Sci. Part A* **2009**, *46*, 521.

[157] M. Xie, D. Fan, Y. Li, X. He, X. Chen, Y. Chen, J. Zhu, G. Xu, X. Wu, P. Lan, *Int. J. Nanomed.* **2017**, *12*, 7751.

[158] M. Beck-Broichsitter, E. Rytting, T. Lebhardt, X. Wang, T. Kissel, *Eur. J. Pharm. Sci.* **2010**, *41*, 244.

[159] S. Kaewpirom, S. Boonsang, *RSC Adv.* **2020**, *10*, 15913.

[160] S. A. L. Matthew, R. Rezwan, Y. Perrie, F. P. Seib, *Molecules* **2022**, *27*, 2368.

[161] J. Kundu, Y. I. Chung, Y. H. Kim, G. Tae, S. C. Kundu, *Int. J. Pharm.* **2010**, *388*, 242.

[162] a) J. I. Solomun, J. D. Totten, T. Wongpinyochit, A. J. Florence, F. P. Seib, *ACS Biomater. Sci. Eng.* **2020**, *6*, 2796; b) M. A. Tomeh, R. Hadianamrei, X. Zhao, *Pharmaceutics* **2019**, *11*, 494.

[163] Z. Toprakcioglu, P. K. Challa, D. B. Morse, T. Knowles, *Sci. Adv.* **2020**, *6*, eaay7952.

[164] N. V. Montoya, R. Peterson, K. J. Ornell, D. R. Albrecht, J. M. Coburn, *Molecules* **2020**, *25*, 890.

[165] J. P. Martins, G. Torrieri, H. A. Santos, *Expert Opin. Drug Delivery* **2018**, *15*, 469.

[166] R. Mukhopadhyay, *Anal. Chem.* **2007**, *79*, 3248.

[167] C. J. Bettinger, K. M. Cyr, A. Matsumoto, R. Langer, J. T. Borenstein, D. L. Kaplan, *Adv. Mater.* **2007**, *19*, 2847.

[168] M. Zhou, X. Shi, X. Li, G. Xiao, L. Liang, J. Ju, F. Wang, Q. Xia, W. Sun, Y. Qiao, L. Yu, Z. Lu, *ACS Appl. Bio Mater.* **2021**, *4*, 8039.

[169] P. M. Valencia, O. C. Farokhzad, R. Karnik, R. Langer, *Nat. Nanotechnol.* **2012**, *7*, 623.

[170] S. J. Shepherd, D. Issadore, M. J. Mitchell, *Biomaterials* **2021**, *274*, 120826.

[171] D. N. Breslauer, S. J. Muller, L. P. Lee, *Biomacromolecules* **2010**, *11*, 643.

[172] Z. Toprakcioglu, A. Levin, T. P. J. Knowles, *Biomacromolecules* **2017**, *18*, 3642.

[173] a) S. P. Kee, A. Gavriilidis, *Chem. Eng. J.* **2008**, *8*, 109; b) M. S. Williams, K. J. Longmuir, P. Yager, *Lab Chip* **2008**, *8*, 1121.

[174] C. Webb, N. Forbes, C. B. Roces, G. Anderluzzi, G. Lou, S. Abraham, L. Ingalls, K. Marshall, T. J. Leaver, J. A. Watts, J. W. Aylott, Y. Perrie, *Int. J. Pharm.* **2020**, *582*, 119266.

[175] J. Hou, H. Ci, P. Wang, C. Wang, B. Lv, L. Miao, G. You, *J. Hazard. Mater.* **2018**, *360*, 319.

[176] M. F. Elahi, G. Guan, L. Wang, *Rev. Adv. Mater. Sci.* **2014**, *38*, 148.

[177] H. B. Yan, Y. Q. Zhang, Y. L. Ma, L. X. Zhou, *J. Nanopart. Res.* **2009**, *11*, 1937.

[178] M. McGill, J. M. Grant, D. L. Kaplan, *Ann. Biomed. Eng.* **2020**, *48*, 1905.

[179] E. S. X. Moh, N. H. Packer, *Biomacromolecules* **2021**, *22*, 1752.

[180] P. Thirumurugan, D. Matosiuk, K. Jozwiak, *Chem. Rev.* **2013**, *113*, 4905.

[181] J. G. Hardy, A. Pfaff, A. Leal-Egana, A. H. Muller, T. R. Scheibel, *Macromol. Biosci.* **2014**, *14*, 936.

[182] K. Spieß, S. Wohlrab, T. Scheibel, *Soft Matter* **2010**, *6*, 4168.

[183] D. Harvey, P. Bardelang, S. L. Goodacre, A. Cockayne, N. R. Thomas, *Adv. Mater.* **2017**, *29*, 1604245.

[184] a) H. Teramoto, K. Kojima, *Biomacromolecules* **2014**, *15*, 2682; b) H. Teramoto, K. Kojima, J. Ishibashi, H. Kajiwara, *Chembiochem* **2012**, *13*, 61.